CANCER

Blocking tumor-intrinsic MNK1 kinase restricts metabolic adaptation and diminishes liver metastasis

Samuel E. J. Preston[1,2], Michael S. Dahabieh[3], Raúl Ernesto Flores González[1,2], Christophe Gonçalves[2], Vincent R. Richard[4], Matthew Leibovitch[5], Eleanor Dakin[1,2], Theodore Papadopoulos[1,2], Carolina Lopez Naranjo[1,2], Paige A. McCallum[1,2], Fan Huang[1,2], Natascha Gagnon[2], Stephanie Perrino[5], René P. Zahedi[4,6,7,8], Christoph H. Borchers[1,2,4,9], Russell G. Jones[3], Pnina Brodt[5,10], Wilson H. Miller Jr.[1,2]*, Sonia V. del Rincón[1,2]*

Dysregulation of the mitogen-activated protein kinase interacting kinases 1/2 (MNK1/2)–eukaryotic initiation factor 4E (eIF4E) signaling axis promotes breast cancer progression. MNK1 is known to influence cancer stem cells (CSCs); self-renewing populations that support metastasis, recurrence, and chemotherapeutic resistance, making them a clinically relevant target. The precise function of MNK1 in regulating CSCs, however, remains unexplored. Here, we generated MNK1 knockout cancer cell lines, resulting in diminished CSC properties in vitro and slowed tumor growth in vivo. Using a multiomics approach, we functionally demonstrated that loss of MNK1 restricts tumor cell metabolic adaptation by reducing glycolysis and increasing dependence on oxidative phosphorylation. Furthermore, MNK1-null breast and pancreatic tumor cells demonstrated suppressed metastasis to the liver, but not the lung. Analysis of The Cancer Genome Atlas (TCGA) data from breast cancer patients validated the positive correlation between MNK1 and glycolytic enzyme protein expression. This study defines metabolic perturbations as a previously unknown consequence of targeting MNK1/2, which may be therapeutically exploited.

INTRODUCTION

Breast cancer (BC) is the most commonly diagnosed cancer among women and the second leading cause of cancer-related death (*1*). For patients with nonmetastatic disease, 5-year survival rates range between 86 and 99% (*2*). However, approximately one-third of patients with BC will present with distant-site metastases, after which the 5-year survival rate is reduced to ~27% (*2*). Prognosis is particularly poor for patients diagnosed with liver metastasis, a common secondary site for BC; even with systemic hormone and/or chemotherapy, median survival is only 20 months (*3*). Stage IV BC is considered incurable with currently available therapies; thus, the ability to reduce BC metastasis remains an unmet clinical need.

Perturbations in mRNA translation are well known to promote cellular transformation and malignant progression (*4*), as exemplified by the mitogen-activated protein kinase interacting kinases 1/2 (MNK1/2)–eukaryotic initiation factor 4E (eIF4E) axis (*5*). eIF4E binds to the 5′ cap of mRNAs to mediate cap-dependent translation. eIF4E is phosphorylated on serine-209 by MNK1/2, encoded by the genes *MKNK1* and *MKNK2* (*6*, *7*). Although the precise function of this phosphorylation event remains unclear in the field, it is clear that MNK-mediated phosphorylation of eIF4E enhances cellular transformation (*8*). Moreover, eIF4E phosphorylation has been well established as promoting disease progression, in part due to the increased translation of a subset of proinvasive and prosurvival mRNAs (*9*–*11*). Our team has published studies demonstrating that phospho-eIF4E–deficient mice are protected against developing lung metastases in both spontaneous and orthotopic models of murine BC (*10*–*12*). In addition, we have explored the multifaceted role of the MNK1/2-eIF4E axis across nontumoral components of the tumor microenvironment (TME), including the immune cell landscape (*11*–*14*) and stromal cell–derived extracellular matrix (*15*). Clinically, the level of phospho-eIF4E has been associated with poor patient prognosis in multiple cancer types (*9*, *16*), encouraging the pharmacological development of MNK1/2 inhibitors that are under clinical testing (NCT05744739 and NCT04622007).

We have previously reported that tumor-intrinsic MNK1 signaling promotes primary BC progression from ductal carcinoma in situ to invasive ductal carcinoma (*17*). This study recognized a link between MNK1 and BC stem cells (BCSCs), showing that modulating MNK1 expression altered BCSC properties in vitro and in vivo. Increasing evidence suggests that BCSCs, a small pool of undifferentiated and self-renewing tumor cells, are the powerhouse behind tumor progression, therapeutic resistance, and metastasis (*18*–*22*). There are several biomarkers, signaling activities, and biological features that define and characterize cancer stem cell (CSC) pools (*23*). In particular, CSCs maintain a remarkable ability to reprogram their metabolic state to adapt to environmental changes (*24*–*26*), which is thought to be critical for their ability to proliferate. Reports from this emerging field implicate glycolysis as a crucial metabolic pathway for CSC populations, including BCSCs, to sustain stemness and self-renewal, and highlight oxidative phosphorylation (OxPhos) and glutamine metabolism as functionally important in some cases (*26*, *27*). While MNK1 has been implicated in regulating stemness (*17*, *28*, *29*), the precise functional role of this kinase in BCSCs, and how this affects metastatic potential to different secondary sites, remains unknown. Metabolic adaptation is especially interesting in

[1]Division of Experimental Medicine, Faculty of Medicine, McGill University, Montréal, QC, Canada. [2]Gerald Bronfman Department of Oncology, Lady Davis Institute for Medical Research, Jewish General Hospital, Montréal, QC, Canada. [3]Department of Metabolism and Nutritional Programming, Van Andel Institute, Grand Rapids, MI, USA. [4]Segal Cancer Proteomics Centre, Lady Davis Institute for Medical Research, Jewish General Hospital, Montréal, QC, Canada. [5]MUHC Research Institute, McGill University Health Centre, Montréal, QC, Canada. [6]Manitoba Centre for Proteomics and Systems Biology, University of Manitoba, Winnipeg, MB, Canada. [7]Department of Internal Medicine, University of Manitoba, Winnipeg, MB, Canada. [8]CancerCare Manitoba, Winnipeg, MB, Canada. [9]Department of Pathology, McGill University, Montréal, QC, Canada. [10]Departments of Surgery, Oncology and Medicine, McGill University, Montréal, QC, Canada.
*Corresponding author. Email: wmiller@ldi.jgh.mcgill.ca (W.H.M.); soniavictoria.delrincon@mcgill.ca (S.V.d.R.)

the context of metastasis given recent findings that highlight tissue-specific metabolic dependencies of metastatic cells. For instance, glycolytic-dominant metabolism can be advantageous for BC metastasis to the liver (*30*), whereas lung metastases rely largely on OxPhos (*31*) and uptake of environmental pyruvate (*32*), and brain metastases require fatty acid synthesis to fuel their growth (*33*).

In this study, we sought to expand our understanding of how MNK1 contributes to BCSC properties. Our results suggest that MNK1 affects BCSC function to affect tumor growth rates in vivo. We performed protein and gene expression analyses, ^{13}C metabolite tracing, and bioenergetic profiling to uncover that MNK1 supports tumor cell glycolysis. Furthermore, we determined that genetic and pharmacologic inhibition of MNK1 restricts tumor cell metabolic adaptability and increases their energetic reliance on OxPhos, resulting in suppressed metastasis to the liver, but not the lung, in breast and pancreatic tumor models. Last, by interrogating mass spectrometry (MS)–derived protein data from The Cancer Genome Atlas (TCGA) PanCancer Atlas Breast Invasive Carcinoma dataset, we demonstrate that MNK1 expression positively correlates with the expression of glycolysis-related enzymes. Together, our findings document the metabolic consequences of disrupting MNK1 in BC cells and highlight the potential utility of MNK1/2 inhibitors as therapeutic agents in targeting tumor metabolism to reduce metastasis.

RESULTS

MNK1 ablation in 4T1 cells alters stemness phenotypes in vitro and in vivo

To better understand the contribution of tumor-intrinsic MNK1 to BC stemness and metastasis, we chose to knock out MNK1 (MNK1 KO) in 4T1 murine BC cells. Using CRISPR-Cas9, we generated and pursued two MNK1 KO cell lines (herein referred to as sg-*MKNK1*-1 and sg-*MKNK1*-2) alongside a single guide RNA (sgRNA)–null control (herein referred to as Cas9CTL). Western blotting confirmed the absence of MNK1 in both KO cell lines, alongside an expected decrease in the phosphorylation of eIF4E (Fig. 1A). 4T1 cell viability was not altered by the loss of MNK1 (Fig. 1B) nor was the proliferative rate under standard monolayer culture conditions (Fig. 1C). We previously showed that phosphorylation of eIF4E, the substrate of MNK1 kinase, promotes epithelial-to-mesenchymal transition (EMT) (*10*). In line with these findings, we found that MNK1 KO 4T1 cells reacquired expression of the epithelial marker E-cadherin concomitantly with reduced expression of mesenchymal markers vimentin and matrix metalloproteinase 3 (MMP3) (Fig. 1D). Given our interest in CSCs and the known link between EMT and development of CSC-like features (*34*), we next chose to culture Cas9CTL and MNK1 KO cells on low-adherence plastic to assess tumorsphere formation from individual cells that maintain the ability to self-renew while avoiding anoikis. While all cell lines tested were able to form spheres, their morphology differed markedly, as MNK1 KO tumorspheres appeared smaller, rounder, and less disordered than Cas9CTL tumorspheres (Fig. 1E). Subsequent quantification confirmed a significant reduction in the average size of sg-*MKNK1*-1 and sg-*MKNK1*-2 tumorspheres compared to Cas9CTL (Fig. 1F), while the number of tumorspheres formed was not altered (Fig. 1G). Next, we used flow cytometry to quantify the expression of CD44 and CD24, two commonly used BCSC markers, across our cell lines under monolayer culture. Although distinct positive and negative populations were not discernible, we found that the mean fluorescence intensity of CD44 was robustly reduced in both MNK1 KO cell lines (Fig. 1H), while only sg-*MKNK1*-2 had reduced CD24 expression (Fig. 1I). In addition, we profiled the impact of MNK1 KO on the activity of aldehyde dehydrogenases (ALDHs), an enzyme group whose activity is enhanced in CSCs (*35*). As expected, MNK1 KO significantly reduced ALDH activity in 4T1 cells as measured by flow cytometry (Fig. 1J). We next assessed whether MNK1 KO cells differ from their control counterparts in tumor outgrowth in vivo. Thus, we injected Cas9CTL and MNK1 KO 4T1 cells into the mammary fat pads of BALB/c mice. Immunohistochemistry (IHC) confirmed that sg-*MKNK1*-1 and sg-*MKNK1*-2 tumors remained devoid of MNK1 expression in vivo (Fig. 1K). Tumors derived from MNK1 KO cell lines grew significantly slower than those from Cas9CTL cells (Fig. 1L). Last, we monitored tumor formation from serially diluted concentrations of Cas9CTL and MNK1 KO cells, a gold standard for assessing stemness. MNK1 KO cells exhibited similar tumor-initiation capacity compared to Cas9CTL cells, even at the lowest cell concentration (Fig. 1M). Coupled with our in vitro observations, the data from this orthotopic model suggest that MNK1 ablation may not dictate the frequency of CSCs within a population but rather the functional capabilities of the CSC pool.

Multiomics analysis highlights alterations in glycolysis and OxPhos pathways in MNK1 KO 4T1 cells

BCSCs are regulated by several major signaling pathways and have multiple biological features that help maintain their activity. We used a multiomics approach to understand the mechanism by which MNK1 ablation regulates 4T1 stem-like behavior. Matched RNA sequencing (RNA-seq) and MS-based discovery proteomics were performed on Cas9CTL, sg-*MKNK1*-1, and sg-*MKNK1*-2 cell lines in quadruplicate (Fig. 2, A and B). Loss of MNK1 resulted in the differential expression of numerous targets at both the RNA (Fig. 2C) and protein level (Fig. 2D), with a large proportion being common to both MNK1 KO clones. As expected, principal component analysis (PCA) revealed genetic and proteomic heterogeneity between our sg-*MKNK1* cell lines (Fig. 2, E and F). At the protein level, sg-*MKNK1* cell lines are more similar to each other than to Cas9CTL (Fig. 2F), particularly when focusing on proteins that are down-regulated in MNK1 KO cells compared to Cas9CTL (see dashed box in Fig. 2B). Downstream validation of differentially regulated targets was limited to expression and phenotype alterations that were consistent across both sg-*MKNK1* cell lines. Functional enrichment analyses were performed to identify biological processes that were commonly differentially expressed between Cas9CTL and MNK1 KO cells (Fig. 2, G and H). Gene set enrichment analysis (GSEA) of our RNA-seq suggested that Wnt and Sonic Hedgehog (Shh) signaling pathways, known to be critical in maintaining BCSC characteristics, were significantly down-regulated in MNK1 KO cells (Fig. 2G and fig. S1A). However, we found no clear direction of regulation in our proteomic data, potentially due to poor coverage of Wnt and Shh signaling components (fig. S1B). Given that dampened Wnt and Shh signaling might help to explain, at least in part, our observations of decreased stem-like properties upon MNK1 ablation, we proceeded with Western blot analysis for several proteins in these pathways. We observed a reduced expression of DVL2 and LRP6, two Wnt signaling mediators, in sg-*MKNK1* cells, while expression of β-catenin was increased (fig. S1C). MNK1 KO cells were further

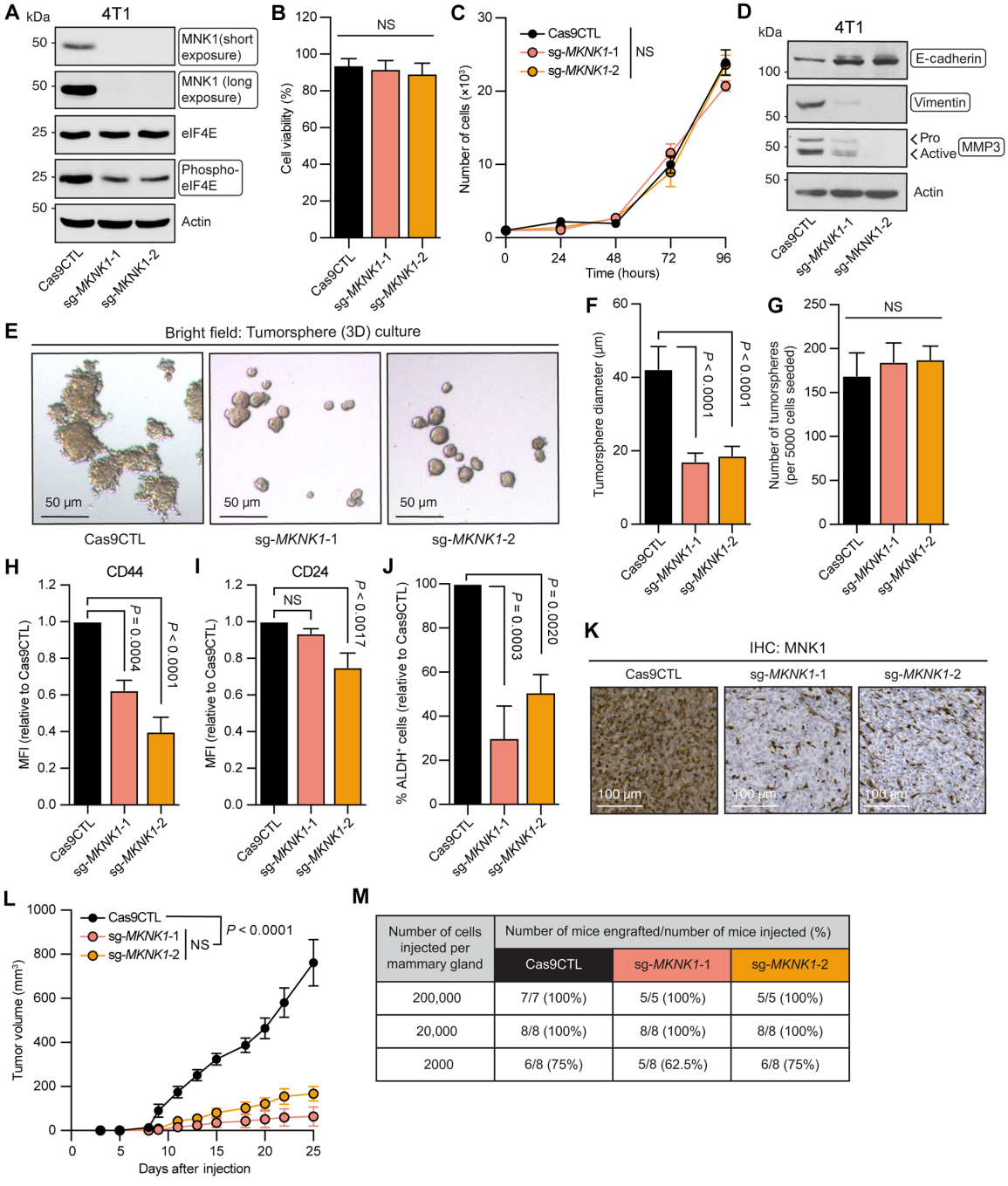

M

Number of cells injected per mammary gland	Number of mice engrafted/number of mice injected (%)		
	Cas9CTL	sg-*MKNK1*-1	sg-*MKNK1*-2
200,000	7/7 (100%)	5/5 (100%)	5/5 (100%)
20,000	8/8 (100%)	8/8 (100%)	8/8 (100%)
2000	6/8 (75%)	5/8 (62.5%)	6/8 (75%)

Fig. 1. MNK1 ablation dampens 4T1 stemness properties. (**A**) Western blotting of the indicated proteins in 4T1 cells. Circled proteins are significantly differentially expressed between cell lines (see fig. S9 for quantification). (**B**) Percentage of live cells of indicated cell lines. Error bars represent SD, one-way analysis of variance (ANOVA) with Tukey's multiple comparison test, $n = 4$. NS, not significant. (**C**) Proliferation of indicated cell lines over 96 hours following serum starvation. Error bars represent SD, two-way ANOVA with Tukey's multiple comparison test, $n = 3$. (**D**) Western blotting of the indicated proteins in 4T1 cells. Circled proteins are significantly differentially expressed between cell lines (see fig. S9 for quantification). (**E**) Representative bright-field images of the indicated cell lines grown under low-adherence tumorsphere culture. 3D, three-dimensional. (**F** and **G**) Average tumorsphere size (F) and tumorsphere number (G) grown from 5000 of the indicated cells. Quantification performed on tumorspheres 7 days after seeding. Error bars represent SD, one-way ANOVA with Tukey's multiple comparison test, $n = 3$ (25 spheres analyzed per cell line per repeat). (**H** and **I**) Average surface expression of CD44 (H) and CD24 (I) in the indicated cell lines. Error bars represent SD, one-way ANOVA with Tukey's multiple comparison, $n = 3$. MFI, mean fluorescence intensity. (**J**) Quantification of ALDH activity in the indicated cell lines. Data represent the percentage of ALDH$^+$ cells relative to Cas9CTL; error bars represent SD, one-way ANOVA with Tukey's multiple comparison test, $n = 3$. (**K**) Representative images of IHC staining against MNK1 [3,3′-diaminobenzidine (DAB)] in indicated tumors. (**L**) Growth rates of tumors formed from the indicated cell lines following mammary fat pad injection. Error bars represent SEM, two-way ANOVA with Tukey's multiple comparison test, $n = 7$ (Cas9CTL) and 5 (sg-*MKNK1*-1 and sg-*MKNK1*-2). (**M**) Number and percentage of mice engrafted following mammary fat pad injection of serially diluted Cas9CTL, sg-*MKNK1*-1, and sg-*MKNK1*-2 cell lines.

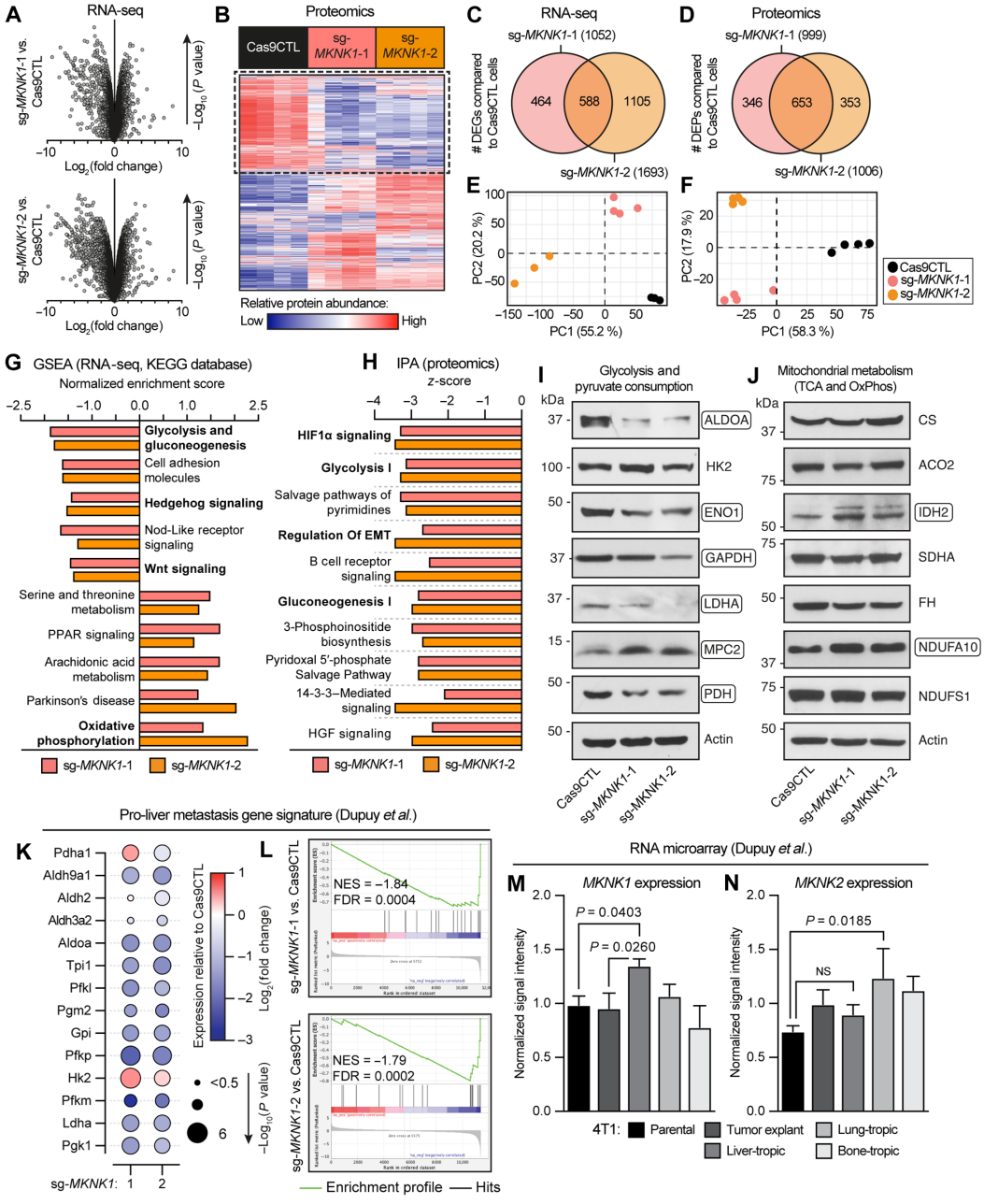

Fig. 2. RNA-seq and proteomic profiling of Cas9CTL and sg-*MKNK1* 4T1 cell lines. (**A**) Volcano plots summarizing differential gene expression as detected by RNA-seq. For RNA-seq data: $n = 3$ (Cas9CTL and sg-*MKNK1*-2) and 4 (*sgMKNK1*-1). (**B**) Heatmap expressing relative abundance values for all proteins identified by MS. For proteomics data, $n = 4$ per group. (**C** and **D**) Venn diagrams depicting the number of differentially expressed genes (DEGs) (C) and differentially expressed proteins (DEPs) (D) between cell lines. (**E** and **F**) PCA of RNA-seq (E) and proteomics (F) datasets. (**G**) GSEA of RNA-seq data through the Kyoto Encyclopedia of Genes and Genomes (KEGG) database. Signatures shown represent the top 5 up- and down-regulated pathways relative to Cas9CTL cells, according to normalized enrichment scores. Only signatures with significant differential regulation (adjusted $P < 0.1$) in both sg-*MKNK1* cell lines are shown. Bar color denotes cell line. PPAR, peroxisome proliferator–activated receptor. (**H**) Ingenuity Pathway Analysis (IPA) of proteomics data in the indicated cell lines relative to Cas9CTL cells. Pathways shown represent the top 10 differentially expressed, irrespective of direction of regulation, according to enrichment *z*-score values. (**I** and **J**) Western blotting of the indicated proteins in 4T1 cells. Circled proteins are significantly differentially expressed between cell lines (see fig. S9 for quantification). (**K** and **L**) Expression of a proliver metastasis gene signature across RNA-seq and proteomics datasets. Proteomics data are shown as a bubble plot (K); color corresponds with expression relative to Cas9CTL, and bubble size corresponds to *P* value. RNA-seq data are shown as GSEA plots (L); normalized enrichment score (NES) and false discovery rate (FDR) values are listed. (**M** and **N**) Expression of *MKNK1* (M) and *MKNK2* (N) in parental, tumor-explant, liver-, lung-, and bone-tropic 4T1 cells. Values acquired from publicly available RNA microarray data. Error bars represent SD, multiple unpaired *t* tests with Welch's correction and Holm-Sidak multiple comparison test, $n = 3$. ACO2, aconitase 2; ADLO, aldolase A; CS, citrate synthase; ENO1, enolase 1; EMT, epithelial-to-mesenchymal transition; FH, fumarate hydratase; GAPDH, glyceraldehyde-3-phosphate dehydrogenase; HGF, hepatocyte growth factor; HK2, hexokinase 2; IDH2, isocitrate dehydrogenase 2; LDHA, lactate dehydrogenase A; MPC2, mitochondrial pyruvate carrier 2; NDUFS1/NDUFA10, NADH:ubiquinone oxidoreductase core subunit S1/subunit A10; PDH, pyruvate dehydrogenase; PPAR, peroxisome proliferation-activated receptor; SHDA, succinate dehydrogenase complex flavoprotein subunit A.

characterized by a reduced expression of smoothened, a critical receptor component of Shh signaling, although the level of repression varied between cell lines (fig. S1C). Given the lack of consistent changes in the expression of Wnt and Shh pathway-related proteins in our cell lines, we did not further pursue this line of investigation.

We instead turned our attention to glycolysis and OxPhos pathways, which were strongly dysregulated in MNK1 KO cells (Fig. 2, G and H). There are two main mechanisms through which cells produce adenosine 5′-triphosphate (ATP) from glucose—glycolysis and OxPhos coupled with the tricarboxylic acid (TCA) cycle (*36*). These include substrate-level phosphorylation during the metabolism of glucose to pyruvate and the generation of reducing equivalents (NADH and $FADH_2$) from glycolysis and the TCA cycle that supply electrons to the electron transport chain (ETC) to fuel ATP generation via OxPhos. Given that our multiomics profiling revealed that sg-*MKNK1* cells differentially regulate these highly linked metabolic processes in opposite directions, we chose to characterize the components of these pathways in more detail. From our GSEA analyses, we observed that both sg-*MKNK1* cell lines significantly repress the glycolysis pathway and up-regulate OxPhos, while the TCA cycle is largely unaltered (fig. S1D). These findings were recapitulated in our proteomic dataset, where we observed a strongly reduced expression of almost all glycolytic enzymes in MNK1 KO cells (fig. S1E). In contrast, the expression of most components of the TCA cycle and ETC remained unchanged or increased. Several subunits of complex I, the first enzyme in the mitochondrial respiratory chain, were robustly up-regulated in MNK1 KO cells (fig. S1E). Western blotting verified the reduced expression of several glycolysis-related enzymes in sg-*MKNK1* cells relative to Cas9CTL (Fig. 2I). In relation to pyruvate consumption, we found that MPC2, which transports pyruvate into mitochondria, was up-regulated in MNK1 KO cells (Fig. 2I). Opposingly, the expression of pyruvate dehydrogenase (PDH), an enzyme that converts pyruvate into acetyl–coenzyme A (acetyl-CoA) for use in the TCA cycle, was reduced in cells lacking MNK1 (Fig. 2I). TCA cycle enzyme expression was largely unchanged between the different cell lines, with the exception of IDH2 which was up-regulated in sg-*MKNK1* cells (Fig. 2J). Last, prompted by our proteomics data (fig. S1E), we validated the up-regulation of the complex I subunit NDUFA10 (Fig. 2J), further suggesting that MNK1 KO cells up-regulate complex I expression. These findings support the conclusion that 4T1 cells lacking MNK1 have rewired their metabolism to depend more on OxPhos. Moreover, these data support the concept that MNK1 KO cells have dampened stemness properties (Fig. 1), as a glycolytic-dominant metabolism has been shown to play a functional role in maintaining BCSC populations (*37*–*39*). Previous work by Dupuy *et al.* (*30*) had further identified a gene signature that underpins high glycolytic activity in 4T1 cells to provide a selective advantage in their ability to metastasize to the liver. We probed the expression of this signature in our Cas9CTL and MNK1 KO cell lines and found that it was significantly reduced in sg-*MKNK1*-1 and sg-*MKNK1*-2 cells at protein (Fig. 2K) and RNA levels (Fig. 2L). In addition, we analyzed publicly available microarray data from Dupuy *et al.* (*30*) [Gene Expression Omnibus (GEO): GSE62598] to compare the expression of *MKNK1* and *MKNK2* across parental 4T1 cells, primary 4T1 tumor–derived explants, and in vivo–selected liver-, lung-, and bone-tropic 4T1 cells. We found that *MKNK1* expression is uniquely up-regulated in liver-tropic cells (Fig. 2M), whereas *MKNK2* is most highly expressed in lung-tropic 4T1 cells (Fig. 2N). Together, these findings suggest a correlation between MNK1 expression in tumor cells and their maintenance of metabolic proliver metastasis features.

Experimental metastasis models demonstrate that MNK1 ablation significantly dampens metastatic tumor outgrowth in the liver, but not the lung

From our multiomics profiling (Fig. 2), we postulated that MNK1 KO 4T1 cells may have a reduced ability to metastasize to the liver. To address this, we performed intrasplenic injections of tumor cells to model experimental liver metastasis (Fig. 3A), as this allows us to robustly replicate the later stages of the metastatic cascade independent of differences in primary tumor growth. We found that mice injected with MNK1 KO 4T1 cells had significantly fewer visible metastases on the liver at 21 days postinjection, compared to their Cas9CTL counterparts (Fig. 3B), leading to a marked increase in mouse survival (Fig. 3C). We further performed an intrasplenic injection of a pool of five independent sg-*MKNK1* 4T1 cell lines to confirm that the observed effect was not an artifact of clonal selection (i.e., individual sg-*MKNK1* clones) and observed a reduction in liver tumor burden in mice injected with the pool of sg-*MKNK1* cell lines (fig. S2A). Western blotting validated that this pool lacks MNK1 expression and subsequently has repressed eIF4E phosphorylation (fig. S2B). To ensure that metastases visible on the surface of the liver were representative of total tumor burden, we performed quantification of hematoxylin and eosin (H&E)–stained step sections of tumor-bearing livers (fig. S2C). As expected, we confirmed that livers harboring MNK1 KO 4T1 cells had a significantly lower number of total metastases (Fig. 3D) and reduced overall percentage tumor burden (Fig. 3E).

Given this robust protection against the development of liver metastases (Fig. 3, B, D, and E), we wanted to understand whether MNK1 KO cells harbor an inability to extravasate out of the vasculature or a failure to colonize and outgrow thereafter. To assess this, we developed an in vivo seeding competition assay whereby an equal ratio of Cas9CTL and MNK1 KO 4T1 cells, each tagged with a different color of CellTracker dye, were intrasplenically injected into the same mouse. Two days after injection, we perfused the liver to flush the vasculature and remove any tumor cells that had failed to extravasate before assessing relative cell abundance by flow cytometry (Fig. 3F). Using this protocol, we demonstrated that neither sg-*MKNK1*-1 nor sg-*MKNK1*-2 4T1 cells had a defect in their extravasation ability when compared to Cas9CTL (Fig. 3G), leading us to conclude that MNK1 plays an important role after extravasation and is required for tumor cell colonization in the extravascular liver microenvironment. To determine whether MNK1 KO cells had a general inability to metastasize, we performed tail vein injections of Cas9CTL and MNK1 KO 4T1 cells (fig. S2D, schematic). MNK1 KO resulted in a mild to nonsignificant reduction in the ability of 4T1 cells to form metastases in the lung, although tumor growth in the liver was severely diminished (Fig. 3H and fig. S2E, representative images). This suggests that the antimetastatic effects of tumor-intrinsic MNK1 ablation are influenced by tissue-specific microenvironments. Next, to further verify the role of glycolysis in MNK1-mediated liver metastasis, we generated a MNK1-addback cell line (termed sg-*MKNK1*-AB). We reexpressed a constitutively active form of MNK1 (*7*) into our sg-*MKNK1*-2 cells, which we compared to their empty vector control counterpart (sg-*MKNK1*-EV). Western blotting confirmed that our MNK1-addback cell line expressed active MNK1, showing an induction of phospho-eIF4E

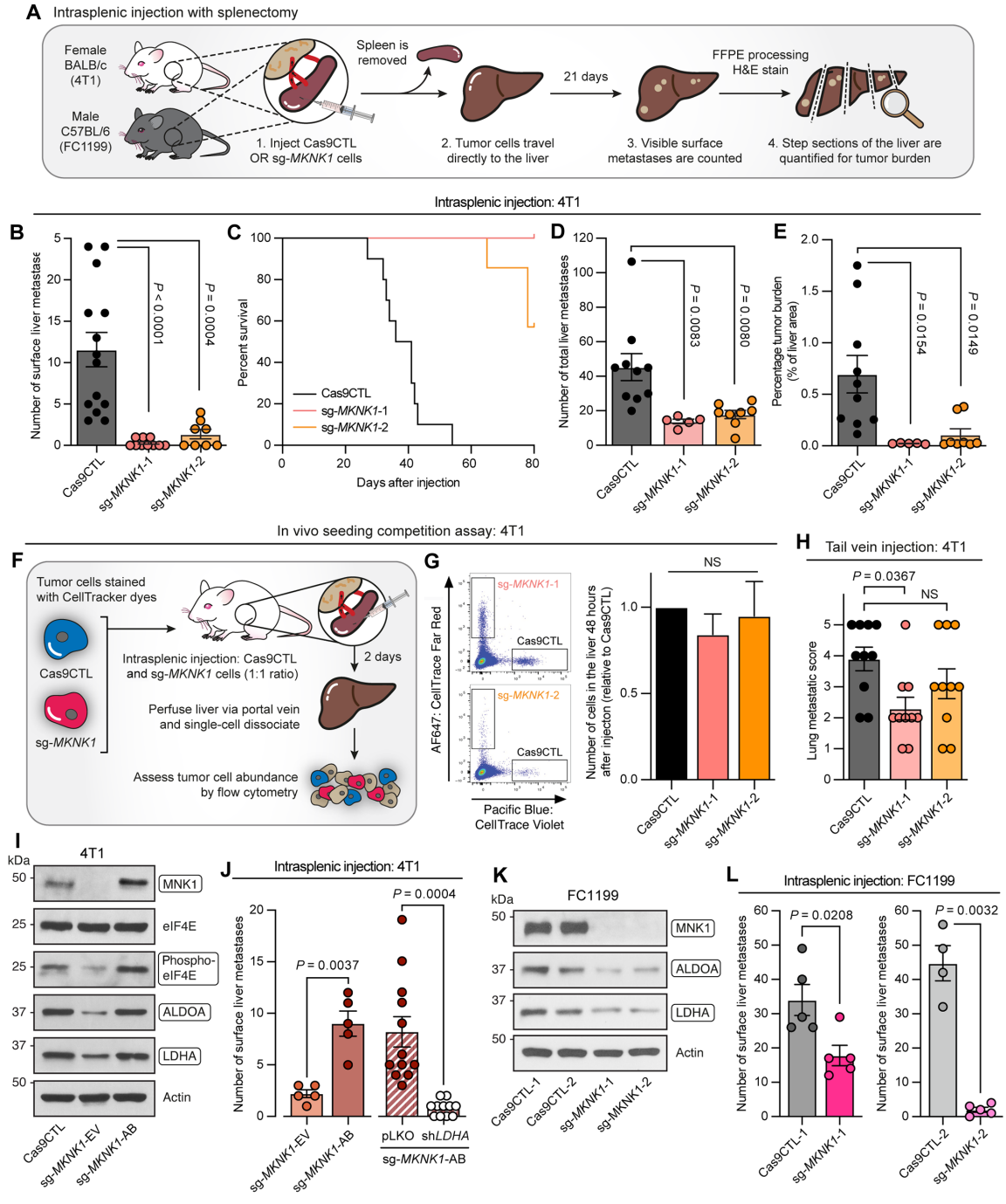

Fig. 3. MNK1-null tumor cells have a reduced ability to form liver metastases. (**A**) Schematic of the intrasplenic injection model. (**B**) Number of metastases visible on the liver 21 days after injection of the indicated cell lines. Error bars represent SEM, $n = 14$ (Cas9CTL), 10 (sg-*MKNK1*-1), and 8 (sg-*MKNK1*-2). (**C**) Kaplan-Meier curves showing mouse survival following intrasplenic injection of the indicated cells. $n = 10$ (Cas9CTL), 8 (sg-*MKNK1*-1), and 7 (sg-*MKNK1*-2). (**D** and **E**) Quantification of tumor burden in H&E-stained liver sections, showing the average number of metastases (D) and percentage tumor area (E). Error bars represent SEM, $n = 10$ (Cas9CTL), 5 (sg-*MKNK1*-1), and 8 (sg-*MKNK1*-2). (**F**) Schematic of in vivo seeding competition assay. (**G**) Representative flow cytometry plots and quantification of Cas9CTL and sg-*MKNK1* cells in the liver 48 hours after injection. Error bars represent SEM, $n = 7$ (Cas9CTL:sg-*MKNK1*-1) and 5 (Cas9CTL:sg-*MKNK1*-2). (**H**) Tumor burden in the lung 14 days after tail vein injection of the indicated cells. Error bars represent SEM, $n = 10$ per group. (**I**) Western blot analysis of the indicated proteins in Cas9CTL, sg-*MKNK1*-EV, and sg-*MKNK1*-AB 4T1 cells. Circled proteins are significantly differentially expressed between cell lines (see fig. S9 for quantification). (**J**) Number of metastases visible on the liver 21 days after intrasplenic injection of the indicated cell lines. Error bars represent SEM, unpaired *t* test with Welch's correction, $n = 5$ (sg-*MKNK1*-EV and sg-*MKNK1*-AB), 12 (pLKO), and 11 (sh*LDHA*). (**K**) Western blotting of the indicated proteins in FC1199 cell lines. Circled proteins are significantly differentially expressed between cell lines (see fig. S9 for quantification). (**L**) Number of metastases visible on the liver 21 days after intrasplenic injection of the indicated cell lines. Error bars represent SEM, unpaired *t* test with Welch's correction, $n = 5$ (Cas9CTL-1, sg-*MKNK1*-1, and sg-*MKNK1*-2) and 4 (Cas9CTL-2). For (B), (D), (E), (G), (H), and (L), one-way ANOVA with Tukey's multiple comparison test was used.

and rescue in the expression of the glycolytic enzymes lactate dehydrogenase A (LDHA) and aldolase A (ALDOA) (Fig. 3I). In vivo, sg-*MKNK1*-AB cells formed significantly more liver metastases compared to their vector controls (Fig. 3J), helping to support the causative role of MNK1 in liver metastasis. If glycolysis underpins this process, then we hypothesized that inhibiting critical glycolytic enzymes, in the MNK1-addback model, would restrict liver metastasis. To test this hypothesis, we used short hairpin RNA (shRNA) to silence *LDHA* in our sg-*MKNK1*-AB cells; a strategy that has been well documented to reduce tumor cell glycolysis (*40*–*42*). Significant knockdown of LDHA, as confirmed through Western blotting (fig. S2F), ablated the ability of our MNK1-addback cells to metastasize to the liver compared to the pLKO vector control cell line (Fig. 3J). These results support the conclusion that MNK1 promotes liver metastasis via up-regulation of glycolytic enzymes, such as LDHA.

Last, we assessed whether ablating MNK1 would affect liver metastasis in other cancer types that are highly liver-tropic. To this end, we generated Cas9CTL and sg-*MKNK1* cell lines using the FC1199 cell line; a well-established model of murine pancreatic ductal adenocarcinoma (PDAC) originally derived from PDAC tumors in KPC (Kras; Trp53; P48-Cre) mice (*43*) on a C57BL/6 background. We performed Western blotting to confirm the MNK1 KO status of this model and observed reduced expression of the glycolytic enzymes ALDOA and LDHA in sg-*MKNK1* FC1199 cells (Fig. 3K), as was shown in our MNK1 KO 4T1 cell lines (Fig. 2I). Similarly, intrasplenic injection of paired Cas9CTL and sg-*MKNK1* FC1199 cell lines phenocopied the protection against liver metastasis that we observed in 4T1 cells, with MNK1 KO cells resulting in significantly fewer metastases on the liver surface at endpoint (Fig. 3L). These data illustrate that targeting MNK1 can reduce liver metastasis across multiple cancer types.

Stable isotope tracing demonstrates that MNK1 KO cells have reduced glycolytic activity and altered glutamine metabolism

There is a growing appreciation that the metabolic state of a tumor cell can dictate tissue-specific tropism and the success of metastatic dissemination. We therefore postulated that the reduced ability of MNK1 KO cells to metastasize to the liver (Fig. 3, B to E, J, and L) could be due to altered cellular metabolism. Given the results of our multiomics functional enrichment analyses (Fig. 2, G and H) and the fact that the liver is a gluconeogenic tissue, we chose to assess functional differences in the use of glucose between MNK1 KO and Cas9CTL 4T1 cells. We performed stable isotope tracer analysis (SITA) using U-[^{13}C]-glucose, incubating cells with the labeled metabolite for 4 hours before MS analysis (Fig. 4A). Results shown in Fig. 4 represent labeled metabolite pool sizes; the full mass isotopomer distribution profiles for all metabolites shown can be found in the Supplementary Materials (figs. S3 and S4). We first assessed several U-[^{13}C]-glucose–derived glycolytic intermediates and end-products in Cas9CTL and MNK1 KO cells (Fig. 4, B to G). While differences in the labeled pool sizes of early-stage glycolytic intermediates glucose-6-phosphate and fructose-1,6-bisphosphate were inconsistent between cell lines (Fig. 4, B and C), sg-*MKNK1* cells had significantly higher levels of labeled (m + 3) glyceraldehyde-3-phosphate (G3P) compared to Cas9CTL (Fig. 4D). Labeled metabolites downstream of G3P, however, were found at significantly lower levels in sg-*MKNK1* cells. These included pyruvate and lactate (m + 3) (Fig. 4, E and F), as well as glycerol-3-phosphate (m + 3), which is synthesized by reducing dihydroxyacetone phosphate (DHAP) after its conversion from G3P (Fig. 4G). These data highlight G3P as a potential bottleneck in the glycolytic chain of MNK1 KO cells (Fig. 4H), in line with the reduced expression of glyceraldehyde-3-phosphate dehydrogenase (GAPDH), enolase 1 (ENO1), and LDHA (Fig. 2I and fig. S9C). In contrast, analysis of the cell culture medium revealed no difference in steady-state labeling of extracellular lactate (Fig. 4I). We hypothesize that the discrepancy between intra- and extracellular lactate labeling may be due to its use as a fuel by 4T1 cells, as one of several physiologically relevant carbon sources (*44*), but future tracing studies are needed to formally test this. In addition to glycolytic products, we observed largely similar levels of the TCA cycle intermediates citrate and malate (m + 2), as well as aspartate (m + 2), which is derived from TCA intermediate oxaloacetate (Fig. 4, J to L). Last, it is likely that both MNK1 KO and Cas9CTL cells also use pyruvate to replenish their pools of TCA intermediates principally through PDH, thereby contributing two labeled carbons into the TCA cycle per pyruvate molecule, rather than through anaplerotic pyruvate metabolism through pyruvate carboxylase, which contributes three labeled carbons per pyruvate. This is evidenced by the higher fractional enrichment of m + 2–labeled citrate and malate compared to m + 3 (fig. S3, H and I). However, note that metabolism of pyruvate through PDH can also yield m + 3–labeled intermediates upon a second turn of the TCA cycle. Overall, these data support that MNK1 ablation in 4T1 cells reduces glycolysis.

Up-regulated glutamine anaplerosis is another key metabolic feature of transformed cells (*45*) and glutamine contributes to regulating redox homeostasis, nucleotide and nonessential amino acid biosynthesis, and epigenetic modifications in CSC populations (*46*). We therefore chose to perform subsequent SITA experiments using U-[^{13}C]-glutamine (Fig. 4M). We observed no significant differences in overall glutamine uptake (Fig. 4N) or conversion to glutamate (Fig. 4O) and no consistent changes in reductive carboxylation as indicated by the fractional enrichment of citrate m + 5 in MNK1 KO cells compared to Cas9CTL (fig. S4C). Both Cas9CTL and MNK1 KO cells use glutamine as an anaplerotic substrate, as indicated by equally labeled pools of malate (m + 4) (Fig. 4P). However, these glutamine carbons were more likely to be used for aspartate synthesis in sg-*MKNK1* cells (Fig. 4Q), while the pool size of labeled citrate was reduced (Fig. 4R). The underlying mechanisms driving these alterations in glutamine metabolism, or their relevance in our model, remain unclear.

Bioenergetic assessment of MNK1 KO cells reveals an energetic dependence on OxPhos

Having demonstrated that MNK1 KO 4T1 cells have reduced levels of glycolytic end-products (Fig. 4, E and F), alongside increased expression of enzymes related to pyruvate consumption and mitochondrial metabolism (Fig. 2, I and J, and fig. S1E), we hypothesized that tumor cells lacking MNK1 may have restricted tumor cell metabolic adaptability. We first assessed broad mitochondrial properties and found that MNK1 KO 4T1 cells have (i) increased mitochondrial mass compared to Cas9CTL (Fig. 5A), as expected by our multiomics analysis (Fig. 2J and fig. S1E), and (ii) greater mitochondrial reactive oxygen species production (Fig. 5B). Next, we performed bioenergetic profiling of Cas9CTL and MNK1 KO 4T1 cells using the Seahorse XF Bioanalyzer platform. We observed no change in

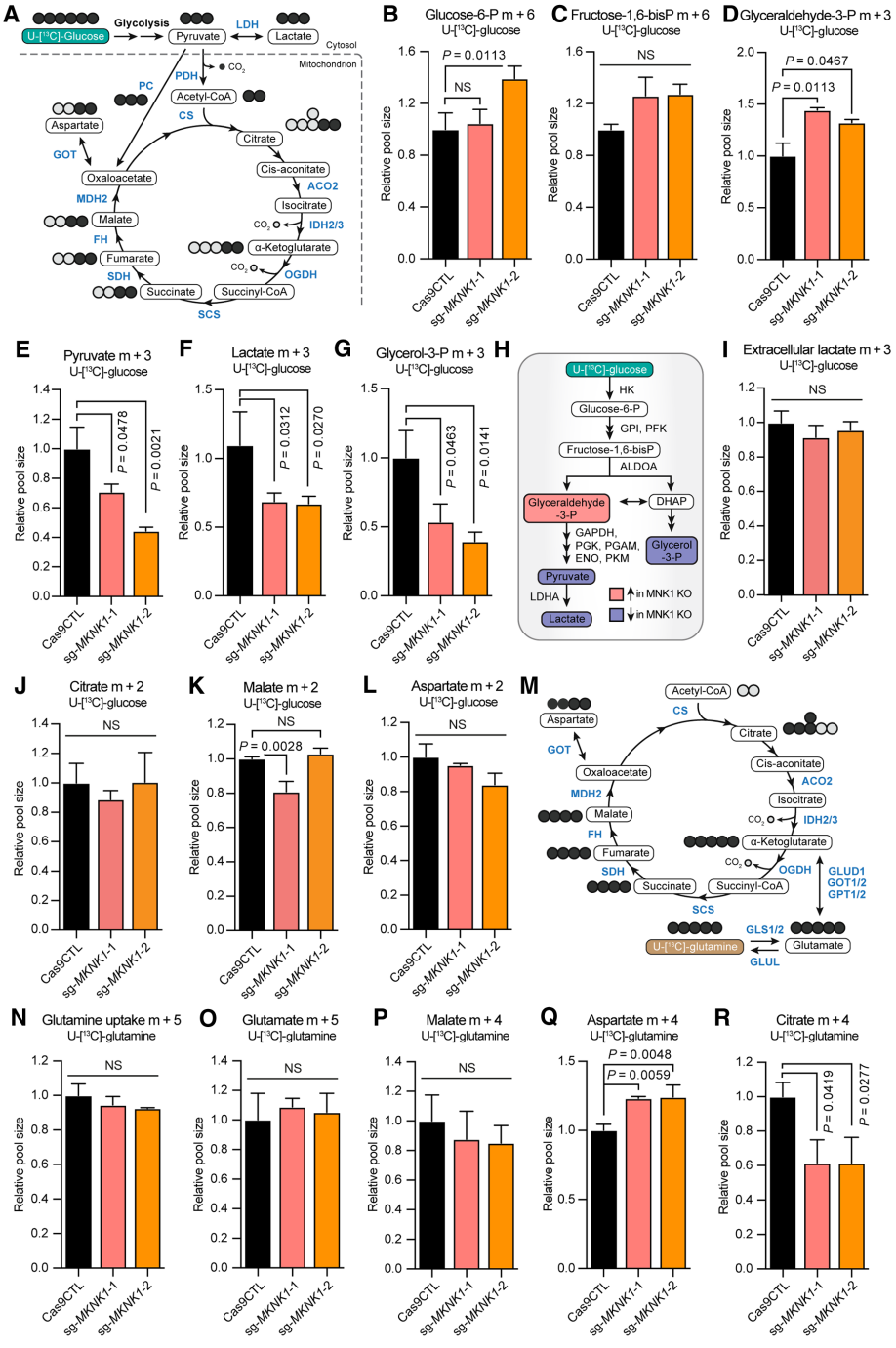

Fig. 4. U-[^{13}C]-glucose and U-[^{13}C]-glutamine SITA of Cas9CTL and sg-*MKNK1* 4T1 cells. (**A**) Stable isotope tracing diagram for U-[^{13}C]-glucose through glycolysis and into the TCA cycle via PDH and pyruvate carboxylase (PC). (**B** to **G**) U-[^{13}C]-glucose tracing into glycolysis (glucose-6-phosphate and fructose-1,6-bisphosphate m + 6, G3P, pyruvate, and lactate m + 3, 4-hour tracer) and glycerol-3-phosphate (m + 3, 4-hour tracer) in the indicated 4T1 cell lines expressed as relative size of the labeled pool. (**H**) Schematic summary of the glycolytic pathway in relation to the data in (B) to (G). (**I**) U-[^{13}C]-glucose tracing into extracellular lactate (m + 3, 4-hour tracer) in the indicated 4T1 cell lines expressed as relative size of the labeled pool. (**J** to **L**) U-[^{13}C]-glucose tracing into the TCA cycle via PDH (citrate, malate, and aspartate m + 2, 4-hour tracer) in the indicated 4T1 cell lines expressed as relative size of the labeled pool. (**M**) Stable isotope tracing diagram for U-[^{13}C]-glutamine into the TCA cycle. (**N** to **R**) U-[^{13}C]-glutamine tracing to glutamate (glutamine uptake and glutamate m + 5, 4-hour tracer) and into the TCA cycle (citrate, malate, and aspartate m + 4, 4-hour tracer) in the indicated 4T1 cell lines expressed as relative size of the labeled pool. For all panels, experiments were performed in technical triplicates and repeated three times. Graphs shown correspond to one representative experiment; error bars represent SD of technical triplicates. Statistics shown were calculated for technical repeats, one-way ANOVA with Tukey's multiple comparison test. DHAP, dihydroxyacetone phosphate; GLS1/2, glutaminase 1/2; GLUD1, glutamate dehydrogenase 1; GLUL, glutamate-ammonia ligase; GOT1/2, glutamic-oxaloacetic transaminase 1/2; GPI, glucose-6-phosphate isomerase; GPT1/2, glutamic-pyruvic transaminase 1/2; MDH2, malate dehydrogenase 2; OGDH, oxoglutarate dehydrogenase; PC, pyruvate carboxylase; PFK, phosphofructokinase; PGAM, phosphoglycerate mutase; PGK, phosphoglycerate kinase; PKM, pyruvate kinase; SCS, succinyl CoA synthase.

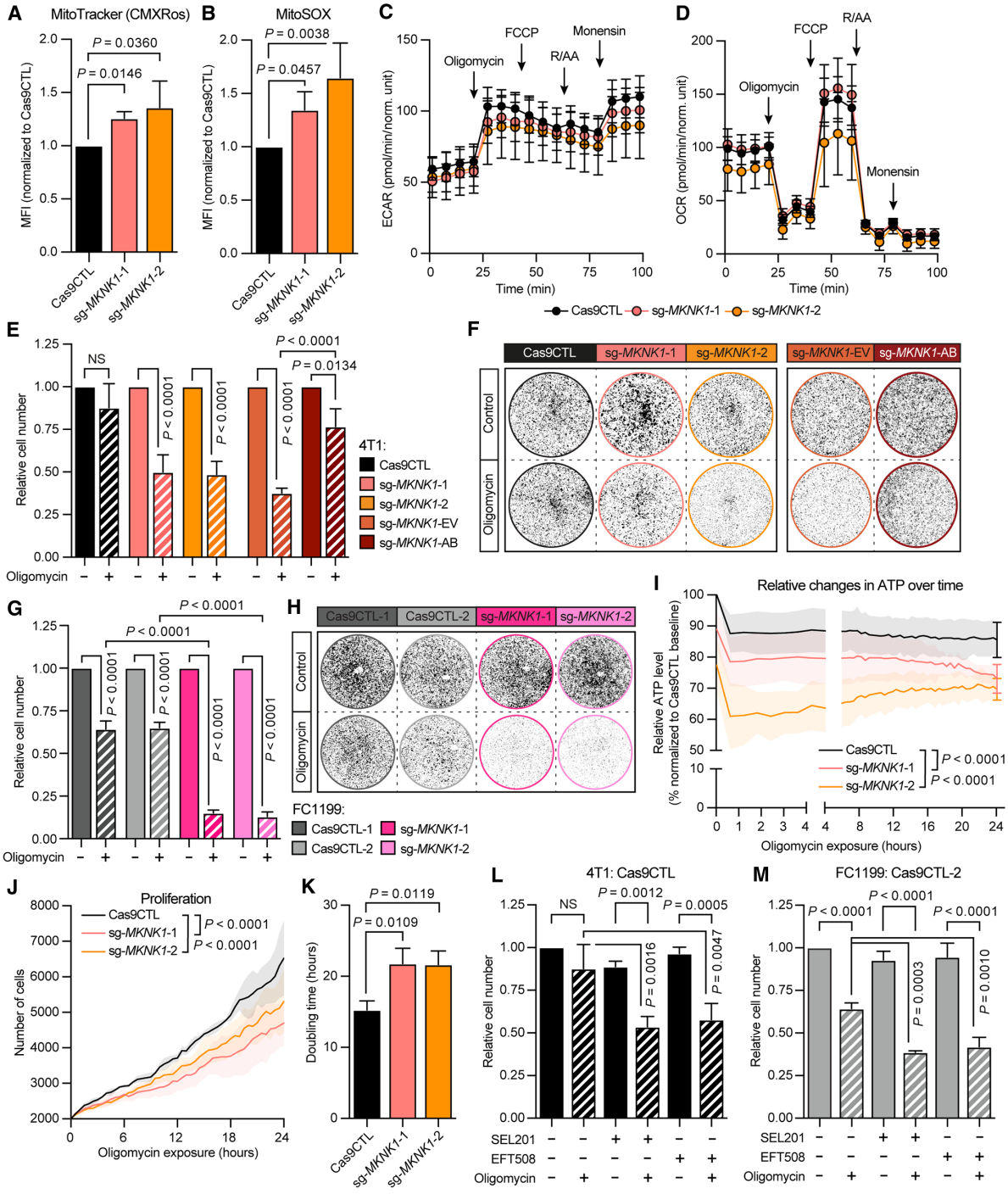

Fig. 5. Bioenergetic assessment of Cas9CTL and sg-*MKNK1* 4T1 and FC1199 cells. (**A** and **B**) Average mitochondrial mass (A) and mitochondrial reactive oxygen species levels (B) of the indicated 4T1 cells. Error bars represent SD, one-way ANOVA with Tukey's multiple comparison test, $n = 4$. (**C** and **D**) Analysis of ECAR (C) and OCR (D) in indicated 4T1 cells, normalized to cell number. Data shown display one representative repeat; error bars represent SD of technical repeats. R/AA, rotenone/antimycin A. (**E** to **H**) Effect of oligomycin (1 μM) treatment on cell growth over 48 hours, relative to a solvent control, in the indicated cells. Oligomycin was removed after 8 hours. Error bars represent SD, two-way ANOVA with Tukey's multiple comparison test, $n = 3$. Representative images are shown in (F) and (H). (**I** and **J**) Relative ATP level (I) and proliferation (J) of the listed 4T1 cell lines over 24 hours of oligomycin (1 μM) treatment under low-glucose conditions (10 mM glucose). Solid lines represent mean value, and shaded areas represent SD. Two-way ANOVA with Tukey's multiple comparison test, $n = 3$ per group. (**K**) Doubling time of the indicated 4T1 cell lines as calculated from data in (J). Error bars represent SD, one-way ANOVA with Tukey's multiple comparison test, $n = 3$. (**L** and **M**) Effect of combining oligomycin (1 μM), SEL201 (2.5 μM), and EFT508 (1 μM) on Cas9CTL 4T1 (L) and Cas9CTL-2 FC1199 (M) cell growth over 48 hours, relative to a no treatment control. Cells were dosed with MNKi for 72 hours total, starting 24 hours before oligomycin treatment. Oligomycin was removed after 8 hours. Data for oligomycin treatment without MNKi are the same as shown in (E). Error bars represent SD, two-way ANOVA with Tukey's multiple comparison test, $n = 3$ per group.

the extracellular acidification rate (ECAR) between MNK1 KO and Cas9CTL cells (Fig. 5C), which is consistent with our SITA results demonstrating no difference in lactate abundance in the medium (Fig. 4I). In addition, there were no differences in oxygen consumption rates (OCRs) across cell lines (Fig. 5D), despite reduced overall production of glycolytic products pyruvate and lactate in MNK1 KO cells. We interpret these findings to suggest that both Cas9CTL and MNK1 KO 4T1 cells, grown under steady-state monolayer culture conditions, primarily use OxPhos to meet their energetic demands, for which our MNK1 KO cells are not disadvantaged. This may explain why MNK1 KO cells (BC and PDAC) exhibited no proliferation defects in vitro (Figs. 1C and 5, F and H).

Next, we chose to assess the metabolic adaptability of Cas9CTL and MNK1 KO cells through use of metabolic inhibitors. Several reports across cancer types demonstrate that metastatic tumor cells in the liver TME favor a glycolytic-dominant metabolism (*30*, *47*–*49*). Thus, we first chose to assess the impact of inhibiting OxPhos in tumor cell cultures, thereby mimicking the metabolic stresses of the liver TME. We found that all MNK1 KO tumor cell lines (sg-*MKNK1*-1 and sg-*MKNK1*-2) were sensitive to treatment with the OxPhos inhibitor oligomycin, resulting in a significant reduction in cell growth, while Cas9CTL cells were unaffected (Fig. 5, E and F). Addback of MNK1 largely reversed this effect, as sg-*MKNK1*-AB cells were significantly less sensitive to oligomycin treatment compared to sg-*MKNK1*-EV cells (Fig. 5, E and F). Encouragingly, these findings repeated in FC1199 MNK1 KO cells. Baseline sensitivity to oligomycin was higher in FC1199 compared to 4T1 cells, but OxPhos inhibition in sg-*MKNK1* cells resulted in a greater repression of cell growth than Cas9CTL (Fig. 5, G and H). Next, we used 2-deoxy-D-glucose (2DG) to inhibit glycolysis and assess its impact on cell growth. We observed no clear effect of MNK1 ablation or addback on 2DG sensitivity, as 2DG inhibited growth by ~25% in all cell lines tested, although this reduction was only statistically significant in Cas9CTL and sg-*MKNK1*-AB cells (fig. S5, A and B). This suggests that the absence of MNK1 sensitizes tumor cells to OxPhos inhibition specifically, which, we propose, is due to the reduced metabolic adaptability of MNK1-null tumor cells. In an environment that selects against an OxPhos-dominant metabolism, we predict that MNK1-null tumor cells are less able to adapt and use glycolysis to generate ATP for proliferation. To investigate this, we performed live-cell ATP imaging in 4T1 Cas9CTL and sg-*MKNK1* cells. Cell lines were engineered to stably express fluorescent ATP indicators that allow for direct measurement of relative ATP levels and treated with oligomycin for 24 hours. As glucose availability is often limited in the TME, unlike standard in vitro culture (25 mM), we also chose to reduce glucose concentrations to more physiologically relevant levels (10 mM) (*44*). Using this approach, we found that MNK1 KO 4T1 cells exhibited significantly lower ATP levels (Fig. 5I), slower proliferation (Fig. 5J), and increased doubling rates (Fig. 5K) compared to their Cas9CTL counterparts. Prolonged oligomycin exposure is likely necessary for these effects, as we observed no differences in OCR between cell lines during short-term oligomycin treatment (Fig. 5D). Combined, these data demonstrate that MNK1 KO 4T1 cells have an impaired ability to use glucose for ATP generation and are particularly disadvantaged in an environment that favors glycolysis over OxPhos, as demonstrated by the impaired growth of MNK1-null tumors in the mammary fat pad and liver (Figs. 1L and 3, B to E, J, and L).

As MNK1/2 inhibitors are currently in clinical trials, we next chose to investigate how well our findings can translate into a therapeutic context. Our team has previously shown that the inhibitors SEL201 and EFT508 effectively block MNK1/2 activity, robustly inhibiting eIF4E phosphorylation (*12*, *13*, *50*, *51*). Western blotting validated that these MNK inhibitors (MNKis) repressed MNK1/2 activity in our 4T1 cells, as indicated by complete repression of phospho-eIF4E, without reducing MNK1 expression (fig. S6A). Inhibiting MNK1/2 kinase activity was insufficient to reduce LDHA expression (fig. S6A). Even at high drug doses, SEL201 and EFT508 were unable to reduce ALDOA or LDHA protein expression (fig. S6B), unlike our cell lines where MNK1 protein expression is ablated (Fig. 2I). Nonetheless, we found that combination treatment of MNKi with oligomycin phenocopied the data obtained in both 4T1 and FC1199 genetic MNK1 KO models, resulting in a significant reduction in tumor cell proliferation compared to either MNKi or oligomycin treatment alone (Fig. 5, L and M). We repeated these assays in three human BC cell lines: T47D, MCF7, and MDA-MB-231. While baseline sensitivity to oligomycin treatment was cell line dependent, the combination of MNKi with oligomycin consistently resulted in significantly repressed cell proliferation compared to oligomycin treatment alone (fig. S6, C to E). Combined MNKi and 2DG treatments further phenocopied our data in the 4T1 MNK1 KO model, as MNK1/2 pharmacologic inhibition did not potentiate the effects of 2DG treatment alone (fig. S6F). Encouraged by these results, we investigated the efficacy of using an MNKi to target liver metastasis in vivo. Mice were predosed with EFT508 immediately before intrasplenic injection of Cas9CTL 4T1 cells, followed by drug dosing until end point (fig. S6G). We observed no difference in mouse body weight changes between EFT508 and vehicle groups (fig. S6H). However, EFT508 treatment alone was insufficient to reduce tumor burden in the liver, as quantified by the number of surface metastases at 21 days after injection (fig. S6I). IHC was performed to confirm that EFT508 was on-target, as indicated by the significant reduction of phospho-eIF4E in liver metastases and the surrounding normal stroma of treated mice compared to vehicle controls (fig. S6J). We next attempted to model dual targeting of MNK1/2 and OxPhos in vivo by combining treatments of EFT508 and IACS-010759, a potent inhibitor of mitochondrial complex I (*52*). Unexpectedly, two-thirds of the mice dosed with IACS-010759 died, presumably because of drug-associated adverse events or toxicity, and the experiment was suspended. In summary, our findings highlight changes in tumor cell metabolism as a previously unknown consequence of using MNK1/2 inhibitors.

MNK1 protein expression correlates with glycolysis in TCGA BC patient data

Our data thus far support that tumor-intrinsic MNK1 signaling regulates glycolysis to promote liver metastasis in preclinical mouse models. To further study the link between MNK1 and glycolysis in human disease, we explored protein data from the PanCancer Atlas Breast Invasive Carcinoma dataset deposited on TCGA. First, we stratified 102 patients by their expression of MNK1, as detected by MS. We then generated clustered heatmaps to compare the relative expression of MNK1 with the expression of proteins involved in glycolysis (Fig. 6A), the TCA cycle (Fig. 6B), and OxPhos (Fig. 6C), as defined by the Kyoto Encyclopedia of Genes and Genomes (KEGG) pathway database. We observed a clear association between high expression of MNK1 and several glycolytic enzymes (Fig. 6A),

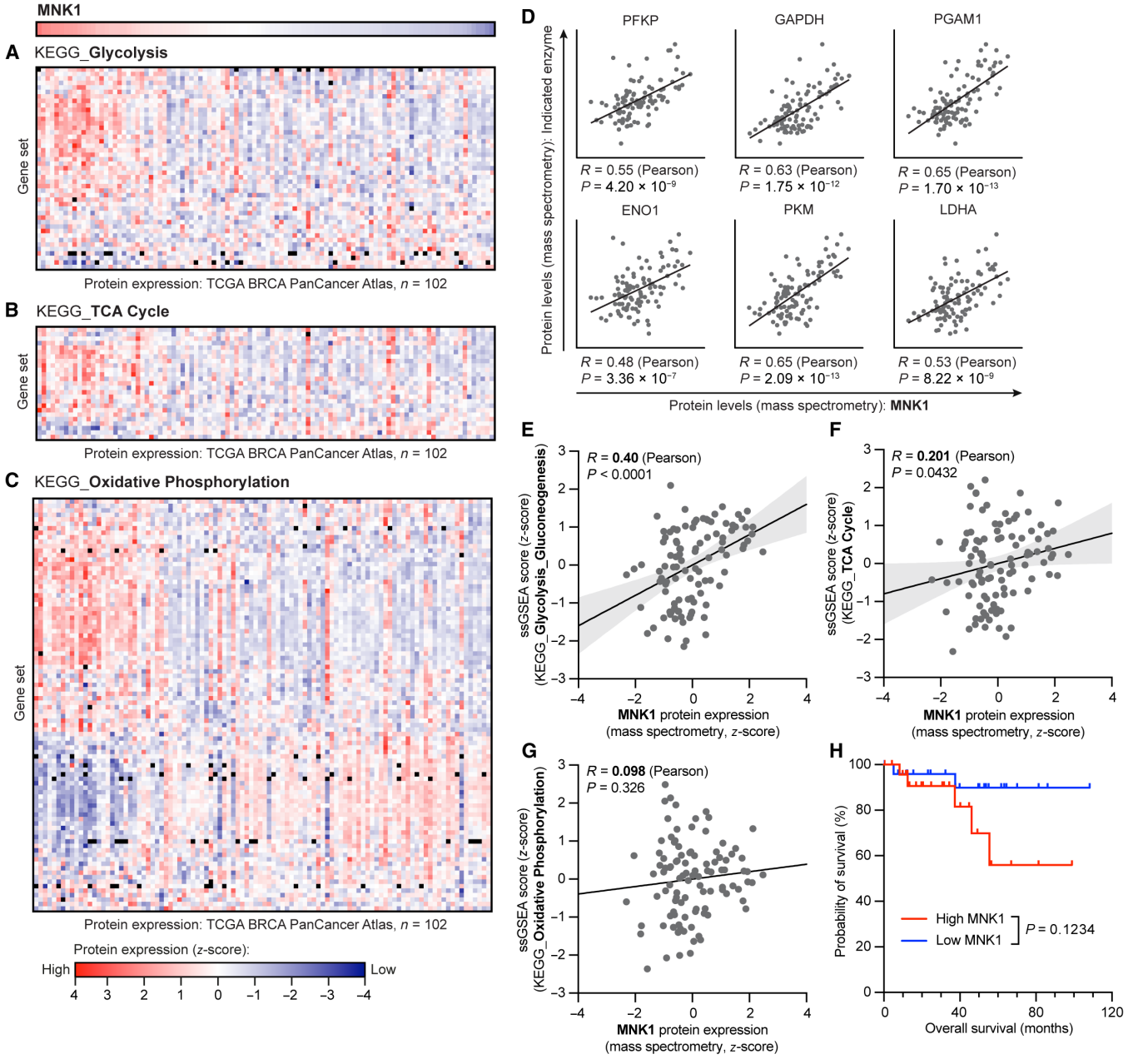

Fig. 6. Analysis of TCGA MS data from patients with BC. (**A** to **C**) Clustered heatmaps visualizing the relative protein expression of MNK1 and glycolysis-related enzymes, as listed in the KEGG glycolysis/gluconeogenesis (A), TCA cycle (B), and OxPhos (C) gene sets. Data are stratified according to MNK1 expression. Each column represents one patient, and each row represents one protein. (**D**) Correlation of MNK1 protein expression with the protein expression of listed enzymes. Pearson rank-order correlation, solid black lines show linear regression. *P* and *R* values are indicated. (**E** to **G**) Correlation of MNK1 protein expression with ssGSEA enrichment scores for the glycolysis/gluconeogenesis (E), TCA cycle (F), and OxPhos (G) pathways. Pearson rank-order correlation, solid black lines show linear regression, and shaded areas represent 95% confidence intervals of the linear regression. *P* and *R* values are indicated. For (A) to (G), $n = 102$. (**H**) Kaplan-Meier curve showing overall survival of patient with high versus low MNK1 protein expression. Log-rank (Mantel-Cox) test, $n = 25$ per group.

including GAPDH, ENO1, and LDHA, which were all observed to be significantly repressed in MNK1 KO 4T1 cells (Fig. 2I and fig. S9C). Analysis of several individual hits identified by our proteomics screening confirmed these correlations, with Pearson coefficients ranging from 0.40 to 0.65 (Fig. 6D). Notably, largely similar correlations were found between MNK2 expression and the same enzymes (fig. S7A). Unexpectedly, we observed a similar association between the expression of MNK1 and TCA cycle enzymes (Fig. 6B), while the pattern for OxPhos was bimodal, with groups of genes that were both positively and negatively correlated with MNK1 expression (Fig. 6C).

To quantify the relationship between the expression of MNK1 and an entire pathway, we performed single-sample GSEA (ssGSEA) projections using the same patient-derived protein data as

above. This involves calculation of an enrichment score per patient, independent of phenotype labeling, which represents the relative activity level of a given biological process rather the expression of a subset of genes. Using this method, we confirmed that MNK1 expression is strongly positively correlated with glycolysis ssGSEA enrichment scores (Fig. 6E) and only weakly correlated with TCA cycle ssGSEA scores (Fig. 6F). We observed an equally strong correlation between glycolysis enrichment scores and the expression of PDK1 (fig. S7B), an enzyme that has been reported to facilitate the adaptation to a glycolytic-dominant metabolism in liver-tropic cells (*30*). In contrast, we found no correlation between MNK1 expression and OxPhos scores (Fig. 6G). These data suggest that MNK1 may support glycolytic activity in tumors from patients with BC, without affecting OxPhos, in line with our own preclinical observations reported herein. We further expanded our analysis to investigate MNK2 and found similar positive correlations between MNK2 expression and glycolysis (fig. S7C) and TCA cycle (fig. S7D) ssGSEA scores. Unlike MNK1, however, we found that MNK2 expression also correlates positively with OxPhos scores (fig. S7E), which aligns with *MKNK2* being up-regulated in lung-tropic 4T1 cells specifically (Fig. 2N). Furthermore, we were intrigued to assess whether our earlier observations regarding Wnt and Shh pathways were recapitulated in patients. Unlike our MNK1 KO 4T1 model, both Wnt and Shh signaling were negatively correlated with MNK1 expression, as shown by clustered heatmap (fig. S8, A and B) and ssGSEA analyses (fig. S8, C and D). Last, although not statistically significant, overall survival of patients with BC can be separated on the basis of MNK1 expression alone, with the high MNK1-expressing group having a numerically worse prognosis compared to the low MNK1 group (Fig. 6H). Together, these results suggest the potential clinical relevance of targeting MNK1 to modulate tumor metabolic features and target tissue-specific metabolic dependencies.

DISCUSSION

CSCs are critical components of successful tumor initiation, progression, and metastasis (*18*–*22*), but our therapeutic tools for targeting these populations in secondary sites remain limited. Defining the molecular mechanisms that underpin CSC populations is therefore critical to design new strategies for metastasis prevention in patients. Here, through our investigation of stemness features regulated by MNK1, we showed that genetic and pharmacological targeting of MNK1 limits the metabolic adaptability of BC and PDAC tumor cells. We found that targeting MNK1 reduced glycolysis, as validated using metabolomic investigation, which increased dependence on OxPhos to meet energetic demands. Hence, dual targeting of MNK1/2 and OxPhos reduced ATP levels and significantly impaired tumor cell proliferation. We showed that this led to strongly repressed primary tumor growth in vivo and almost entirely abolished metastasis to the liver, but not the lung. Last, we have shown that MNK1 expression is positively correlated with expression of the glycolytic pathway in samples of human patients with BC.

This study sheds light on the signaling pathways that contribute to the complex changes in cell metabolism that facilitate metastasis. The Warburg effect predicts that most cancer cells rely on aerobic glycolysis to fuel their proliferation (*36*). It is thought that BCSC populations are largely driven by high rates of glycolysis (*24*), at least in the primary site. One study even demonstrates that a metabolic switch from OxPhos to aerobic glycolysis is essential for the function of BCSCs and enhances tumorigenicity in vitro and in vivo (*38*). The data presented here support this conclusion as MNK1 KO 4T1 cells, with reduced glycolytic activity, have significantly reduced rates of primary tumor growth (Fig. 1L). Our knowledge of the metabolic processes that dictate metastatic outgrowth and tropism, however, is less advanced. The "seed and soil" theory, alongside more recent work by Schild *et al.* (*53*), proposes that specific cancer cells evolve to have distinct metabolic signatures that predetermine their propensity to colonize a distant tissue. Furthermore, it has been suggested that only cells with metabolic adaptability, a hallmark of CSCs, have the intrinsic ability to survive in secondary sites (*54*). Some studies have even provided evidence for organ-specific metastatic abilities of CSC subpopulations in multiple cancers (*49*, *55*, *56*). Although this study does not assess the metabolic function of CSCs specifically, we predict that the restricted metabolic adaptability caused by targeting MNK1 would be disadvantageous to CSC and non-CSC pools alike. Moreover, we show that this disadvantage is not equal across metastatic sites; targeting MNK1 in 4T1 cells more strongly reduced their abundance in the liver than in the lung (Fig. 3, B to E and H), independent of their ability to extravasate from the vasculature (Fig. 3G) but underpinned by their ability to perform glycolysis (Fig. 3J). Our data support a model in which a tumor cell that lacks MNK1 is less able to adapt its metabolic program to be compatible with the microenvironment of its target organ. A metastatic tumor cell that seeds in the lung, an environment rich in oxygen and oxidative stress, will use OxPhos to outgrow. In contrast, a tumor cell that colonizes the liver, a tissue that regulates glucose consumption/storage and is more likely to be hypoxic, must be able to generate ATP from glucose to thrive. Thus, the liver microenvironment would be predicted to be disadvantageous for the survival of MNK1-null tumor cells. This may explain why we observed different effects of MNK1 ablation on tumor cell growth in two-dimensional versus three-dimensional cultures, as tumorspheres are enriched in BCSCs (highly glycolytic) compared to monolayer culture. Future metabolomics studies on tumorsphere cultures would be needed to assess this directly.

Similarly, when expanding our findings into models of PDAC metastasis, we observed that targeting of MNK1 also reduced glycolytic enzyme expression and metastasis to the liver (Fig. 3, K and L). This aligns well with the seminal study by Ying *et al.* (*57*), which demonstrated how PDAC progression is driven by KRAS-mediated activation of anabolic glucose metabolism and that targeting this pathway led to the emergence of treatment-resistant CSC-like cells with an OxPhos-dominant metabolism (*58*). As in BC, more recent work has suggested that two subsets of CSCs exist in PDAC; one forms lung metastases through primarily oxidative metabolism, while the other forms liver metastases through aerobic glycolysis and fatty acid oxidation (*49*). As the liver is the primary site of PDAC metastasis and liver metastases are a major cause of PDAC-related death, understanding the molecular drivers underpinning metastatic outgrowth in the liver is crucial to the design of targeted therapeutics that can prevent metastatic disease. It is unknown whether the control of glycolysis by MNK1 is relevant in cancer types other than BC and PDAC. In contrast to the findings of this study, we have previously shown that MNK1 ablation in melanoma cell lines significantly reduced their ability to metastasize to the lung following tail vein injection (*51*), suggesting that the contribution of MNK1 to metastasis varies between diseases. More work is needed to clarify the differences in metabolic programs between cancer

types and cell lines. Nevertheless, our findings support the exploration of MNK1 as a therapeutically relevant target for populations of cells that rely on glycolytic metabolism, rather than a specific disease model or subtype. Beyond glycolysis, the MNK kinases have been shown to play roles in cellular lipid metabolism in the context of high-fat diet–induced obesity, including control of triglyceride turnover and the translational regulation of genes that dictate lipid transport and storage (*59*, *60*). Furthermore, it has been demonstrated that several genes associated with mitochondrial biogenesis are up-regulated in the adipose tissue of MNK1/2 double KO mice compared to wild type (*59*), in line with our observation that sg-*MKNK1* cells have increased mitochondrial mass compared to Cas9CTL cells (Fig. 5A). In contrast, we observed no correlation between MNK1 and OxPhos in our analysis of patient proteomic data (Fig. 6, C and G) and no significant difference in 2DG sensitivity between MNK1-expressing and MNK1-null cells (fig. S5A). It therefore may also be true that the up-regulation of ETC-related subunits in MNK1 KO 4T1 cells (Fig. 2J and fig. S1, D and E) is a necessary consequence of down-regulated glycolysis rather than a direct result of MNK1 ablation. Continued work is therefore needed to better understand what role MNK1/2 plays as a regulatory node of cellular metabolism.

Our analysis of protein expression data from patients with BC (Fig. 6) suggests that targeting MNK1 to affect tumor cell metabolism may translate from murine to human studies. We show that genetic MNK1 KO models of BC are protected against metastatic outgrowth in the liver (Fig. 3, B to E and J), but use of EFT508 alone was unable to phenocopy this result (fig. S6I). We hypothesize that there may be unknown consequences of broadly blocking MNK activity across the TME using a MNK1/2 inhibitor, as opposed to the more specific tumor–intrinsic targeting of our genetic model. In particular, although a critical role for mRNA translation control in nontumor components of the TME is emerging (*61*), it is yet to be determined how blocking MNK pharmacologically affects the cooperative metabolic networks that exist between cell types of the TME or how MNKi-mediated disruption of glycolysis affects immune cell function. Further research is required to better understand these interactions. However, we have shown in vitro that blocking MNK1 increases tumor cell sensitivity to oligomycin and that combined treatment with MNKi significantly reduced tumor cell growth in multiple cancer cell lines (Fig. 5, L and M, and fig. S6, C to E). It may therefore be necessary to combine an MNKi with an OxPhos inhibitor to adequately restrict the metabolic adaptability of tumor cells in vivo, even in the liver microenvironment. We propose this drug combination as a potential strategy to target metastases by simultaneously affecting the two primary mechanisms of ATP production. This is a crucial target in metastasizing tumor cells as sufficient ATP generation is emerging as a critical threshold for successful cell seeding (*62*). MNKi are well tolerated in patients and are currently under clinical investigation across cancer types and treatment modalities (NCT04261218, NCT03690141, and NCT04622007). Several drugs targeting aspects of mitochondrial metabolism are either already Food and Drug Administration–approved or in clinical trials, including metformin (*63*, *64*) and atovaquone (*65*). However, clinical benefit of these inhibitors is yet to be achieved in the context of oncology. We performed preclinical studies using combined treatment of EFT508 and the complex I inhibitor IACS-010759, which was advanced into phase I clinical trials at the time (NCT02882321 and NCT03291938). These trials were recently discontinued because of emerging dose-limiting toxicities, including neuropathy in ~50% of patients and physiological changes indicative of neuropathy in mice (*66*). This agrees with our observation that IACS-010759 led to toxicity in our mouse models. Future studies are therefore needed to assess how to effectively combine MNKi and OxPhos inhibition and to determine at what stage of the metastatic cascade these drugs could be applied for clinical benefit.

Study limitations

One question that remains unanswered in our study is as follows: By what mechanism does blocking MNK1 down-regulate glycolysis? Although eIF4E is the only validated substrate for MNK1/2 kinases, we do not assess whether the phenotypes we observe are a consequence of altered translational control by phospho-eIF4E. It is conceivable that there are eIF4E-independent effects of modulating MNK expression and/or activity that are yet to be identified. Moreover, a mechanism involving the regulation of selective mRNA translation may exist either directly or indirectly. Phospho-eIF4E may regulate the translation of glycolytic enzymes themselves or that of an upstream mediator such as hypoxia-inducible factor 1α (HIF1α), as was emphasized by our proteomics data (Fig. 2H). The EMT-associated protein Snail, known to be under translational control of phospho-eIF4E (*10*), has been shown to silence the promoter of *FBP1*, resulting in an induction of glycolysis and CSC-like properties in basal-like BC (*38*). Future studies are needed to determine which of these mechanisms, if any, are at play in our models. Regardless, this study highlights MNK1 within an ever-expanding body of literature that defines translational machinery as a central node for regulating energetic balance and cellular metabolism (*67*–*71*).

Our comparison of genetic KO and kinase inhibition of MNK1 was unsuccessful in shedding light on these mechanistic details. MNK1-null tumor cells are more sensitive to OxPhos inhibition than MNK1-expressing cells (Fig. 5E), a phenotype that is recapitulated through combined treatment of oligomycin and pharmacologic MNK1/2 inhibition (Fig. 5L). Furthermore, ablation of MNK1 reduced glycolytic enzyme expression at the protein level (Fig. 2I), which was rescued upon MNK1 addback (Fig. 3I). In contrast, low- and high-dose treatments with MNKi were insufficient to reduce enzyme expression, at least LDHA and ALDOA (fig. S6, A and B). In patient populations, however, the correlation between MNK1 and glycolytic enzyme expression is clear. The reason for this discrepancy between genetic and therapeutic models remains unknown. One explanation is that without a clear mechanistic understanding of this regulation, we chose inappropriate readouts to address this question. Alternatively, it is plausible that we must target MNK1 protein expression, rather than kinase activity, to repress glycolytic enzyme expression. This could explain why EFT508, which binds competitively with ATP to block MNK1/2 kinase activity, was unable to reduce liver metastasis in vivo despite reducing eIF4E phosphorylation (fig. S6, I and J). Similar conclusions have been drawn from studying the role of MNK2 in adipocyte differentiation, where genetic knockdown of MNK2 perturbed lipid synthesis and accumulation, while treatment with EFT508 did not (*72*). It therefore seems likely that MNK1/2 have kinase-independent functions that remain unknown. Advances in technologies such as proteolysis targeting chimera (*73*), or the recently identified VNLG-152R that degrades MNK1/2 (*74*), may improve the viability of targeting these kinases to augment anticancer therapeutic outcomes.

Last, this study is limited in its investigation of the MNK2 kinase. We chose to assess the impact of ablating tumor-intrinsic MNK1 specifically, due in part to the understanding that MNK1 activity is induced by extracellular stimuli, whereas MNK2 activity is constitutive (*75*, *76*). We assume that the low levels of phospho-eIF4E in sg-*MKNK1* cells are a result of MNK2-mediated phosphorylation, but a lack of reliable antibodies to detect MNK2 specifically makes it difficult to assess this directly in our model. Our RNA microarray analysis revealed that 4T1 cells up-regulate specific MNK isoforms based on the secondary site that they have been selected to metastasize to (Fig. 2, M and N). Furthermore, patient-derived proteomic data highlight that MNK1 and MNK2 expressions correlate equally with glycolysis ssGSEA scores (Fig. 6E and fig. S7C), whereas only MNK2 significantly correlates with OxPhos ssGSEA scores (fig. S7E). These data may suggest that both MNK1 and MNK2 can regulate glycolysis, whereas regulation of OxPhos may be MNK2 specific. However, future studies are needed to assess this directly. Generating tumor-intrinsic MNK2 KO and MNK1/2 double KO cell lines will help to provide the tools needed to study isoform-specific contributions of the MNK1/2 kinases to cellular metabolism and metastasis.

In conclusion, this study supports the utility of targeting metabolic pathways as strategies to reduce metastasis. We have gained an increased understanding of the contribution that MNK1 kinase makes in controlling CSC populations, while further identifying reduced glycolysis as a previously unknown functional consequence of targeting MNK1/2. Better understanding of the metabolic dependencies of metastatic tumor cells in tissue-specific microenvironments may prove useful in identifying vulnerabilities that can be exploited, through use of MNK-targeting therapeutics, to improve therapeutic efficacy.

MATERIALS AND METHODS

Cell culture and treatments

4T1 cells were donated by P. Siegel (McGill University). FC1199 cells were gifted from the Tuveson laboratory (Cold Spring Harbor Laboratories) and obtained in collaboration with A. Lowy (University of California San Diego, La Jolla) and P. Brodt (McGill University). MCF7, T47D, and MDA-MB-231 cell lines were purchased from American Type Culture Collection. 4T1 cells were cultured in Dulbecco's modified Eagle's medium (DMEM) high glucose (Wisent Bioproducts) supplemented with 10% fetal bovine serum, sodium bicarbonate (1.5 g/liter), 10 mM Hepes, and antibiotics. All other cell lines were cultured in DMEM high glucose (Wisent Bioproducts) supplemented with 10% fetal bovine serum and antibiotics. Cells were subcultured upon reaching ~90% confluence by trypsinization and subsequent dilution. Cell lines were maintained at low passage number before use, and viability was determined via trypan blue exclusion. For all cell treatments, drugs were supplemented into complete growth medium at the indicated concentrations. SEL201 was provided by Selvita and used at 2.5 μM. EFT508 (tomivosertib) was purchased from Selleckchem (#S8275) and used at 1 μM. Oligomycin was purchased from MP Biomedicals (#151786) and used at 1 μM. 2DG was purchased from MedChemExpress (#HY-13966) and used at 1 mM. For tumorsphere culture, cell lines were trypsinized, dissociated into single cells, and seeded in six-well plates with ultralow adherence (Corning, #3471) at 5000 cells per well. Bright-field images were captured at 5 days after seeding. Tumorsphere number and size were quantified using ImageJ.

Generation of MNK1 KO, addback, and shRNA cell lines

CRISPR-mediated MNK1 KO cell lines were generated as previously described (*17*). In summary, parental 4T1 cells were transfected with Cas9–green fluorescent protein (GFP)/sgRNA plasmids. Forty-eight hours after transfection, GFP^+ cells (transient fluorescence) were single cell–sorted by fluorescence-activated cell sorting and expanded in culture. The resulting clones were screened for absent expression of MNK1 by Western blot, and selected clones were further validated by Sanger sequencing of genomic DNA. Two clones were selected for follow-up investigation in vitro and in vivo, termed sg-*MKNK1*-1 and sg-*MKNK1*-2 4T1. A sgRNA-null control cell line was generated using the same transfection protocol with the Cas9-GFP plasmid only, termed Cas9CTL. MNK1 KO FC1199 cell lines were generated using the same protocol, plasmid constructs, and sgRNA sequences. For the 4T1 model, two sg-*MKNK1* cell lines were compared to the same Cas9CTL line. For the FC1199 model, pairs of Cas9CTL and sg-*MKNK1* cell lines were generated and compared separately. Where indicated, a pool of five sg-*MKNK1* 4T1 clones were combined together in equal proportions (20% of the total cell population per clone). Plasmids and sgRNA constructs were purchased from GenScript, using the pSpCas9 BB-2A-GFP (PX458) vector. Two CRISPR guide RNA sequences were designed to target murine *MKNK1*: TCGAAGTCGAGTGTTCCGTG and GACGTCCCGCACCACTCTAC. sg-*MKNK1*-2 4T1 cells were further engineered to express a constitutively active form of MNK1 ($MNK1^{T332D}$) or the corresponding empty vector control. Transduced cells were selected for puromycin resistance to yield sg-*MKNK1*-AB and sg-*MKNK1*-EV cell lines. The MNK1-addback cell line was subject to additional genetic manipulation using shRNA. Using our previously described protocol (*77*), sg-*MKNK1*-AB cells were transduced with a combination of two shRNA constructs targeting *LDHA* (*Mus musculus* NM_010699.2; TRCN0000308704/TRCN0000308638) or a pLKO.5 control vector. Puromycin-selected cells were used for downstream investigation. The efficiency of the LDHA knockdown in the MNK1-addback cells was validated by Western blotting.

Mouse models and orthotopic mammary fat pad injection

Wild-type BALB/c and C57BL/6 N mice were purchased from Charles River Laboratories (Saint-Constant, Canada) and subsequently bred in-house. All tumor cell injections were performed on mice approximately 8 to 10 weeks of age. Animal experiments were conducted according to the regulations established by the Canadian Council of Animal Care, using protocols approved by the McGill University Animal Care and Use Committee (Acceptable Use Policy numbers: 6009 and 5260). For orthotopic injections, 2×10^5 4T1 cells (Cas9CTL or sg-*MKNK1*) were suspended in phosphate-buffered saline (PBS) and injected into the inguinal mammary fat pad of BALB/c mice. Tumor initiation was measured as the number of days after injection at which a palpable mass had formed. Tumor length (L) and width (W) were routinely measured over time, with tumor volume calculated using the formula $V = 3.1416/6 \times L \times W^2$. At 25 days after injection, mice were euthanized, and primary tumors were excised, formalin-fixed, and paraffin-embedded (FFPE). For the limiting dilution experiment, serially diluted concentrations (2×10^5, 2×10^4, and 2×10^3) of Cas9CTL and sg-*MKNK1* 4T1 cells were suspended in PBS and injected into the inguinal mammary fat pad of mice. Tumors were allowed to form for 8 weeks after injection until a palpable mass was detected (engrafted).

Experimental metastasis mouse models: Intrasplenic and tail vein injections

Intrasplenic injections (with splenectomy) were used to model experimental liver metastasis. Mice were anaesthetized, hair on the left flank was removed, and a small incision was made in the skin and peritoneum below the ribcage. A total of 1×10^5 (4T1) or 2×10^5 (FC1199) cells (Cas9CTL, sg-*MKNK1*, MNK1-addback, or shRNA-manipulated) were suspended in PBS and injected directly into the spleen of female BALB/c (4T1) or male C57BL/6 (FC1199) mice using a 26-gauge needle. Cells travel via the splenic vein and hepatic portal vein directly to the liver. Following injection, vasculature connecting the spleen and the pancreas was ligated using nonabsorbable braided silk suture (Fine Science Tools, #18020-60). Vessels were subsequently cut, and the spleen was removed—this is necessary to prevent the formation of a primary splenic tumor. The peritoneum was then sutured shut and the skin closed using wound clips. Mouse body weight was monitored every 3 to 4 days, before being euthanized at 21 (4T1) or 22 (FC1199) days after injection. At end point, the number of metastases visible on the liver surface was quantified before FFPE processing. Mice with extrahepatic metastases were excluded from the study. For survival cohorts, mice were euthanized upon signs of moribundity or a 20% drop in body weight, whichever presented first. For treatment cohorts, mice were randomly grouped before treatment. EFT508 was dissolved in a solution of 10% 1-methyl-2-pyrrolidinone and 90% propylene glycol, with one equivalent of HCl, for administration by oral gavage at a dose of 10 mg/kg of body weight per mouse, five times per week. The first dose was administered ~1 hour before intrasplenic injection. Tail vein injections were used to model experimental lung metastasis; 1×10^5 4T1 cells (Cas9CTL or sg-*MKNK1*) were injected into the tail vein of each mouse. At 14 days after injection, mice were euthanized, and lungs were excised and dissociated into single cells using the gentleMACS Octo Dissociator (Miltenyi Biotec, #130-096-427). Cell suspensions were cultured in the presence of 30 μM 6-thioguanine (Sigma-Aldrich, #A4660); these conditions are toxic to cells other than the naturally resistant 4T1. After 5 days, remaining 4T1 colonies were fixed with 4% paraformaldehyde (PFA) for 15 min at room temperature and stained with 0.5% crystal violet for 30 min at room temperature, and metastatic burden was scored by four independent individuals.

In vivo seeding competition assay

4T1 cells (Cas9CTL and sg-*MKNK1*) were labeled using CellTrace Violet (Invitrogen, #34571) or Far Red (Invitrogen, #C34564) dyes according to the manufacturer's instructions before intrasplenic injection. Each mouse received a total of 1×10^6 cells composed of one MNK1 KO clone and Cas9CTL cell lines at a 1:1 ratio, with each cell line labeled using a different color of CellTrace dye. At 48 hours after injection, mice were euthanized, and the liver perfused via the hepatic portal vein with 15 ml of cold PBS. Following this, livers were excised and single cell–dissociated using the gentleMACS Octo Dissociator (Miltenyi Biotec, #130-096-427). Cell suspensions were then analyzed on an LSRFortessa (BD Biosciences) for the presence of fluorescent tumor cells.

RNA-seq and analysis

RNA was isolated from Cas9CTL and sg-*MKNK1* 4T1 cell pellets in quadruplicate using the Absolutely RNA Miniprep Kit (Agilent Technologies, #400800). RNA concentration and quality were assessed using a Bioanalyzer (Agilent Technologies). Note that the RNA quality for one sg-*MKNK1*-2 technical replicate was below threshold and this sample was therefore excluded. Library preparation was performed using the KAPA mRNA HyperPrep Kit (Roche). Samples were sequenced on a NextSeq High-Output 2× 75–base pair flow cell with a yield of ~20 M single-end reads per sample. FASTQ data were normalized using the Nextflow nf-core pipeline (DOI: 10.5281/zenodo.1400710) and expressed as log-transformed counts per million reads mapped ($\log_{10}$CPM). The DESeq2 R package was used to identify differentially expressed genes by calculating the fold change in $\log_{10}$CPM values between MNK1 KO (sg-*MKNK1*-1 or sg-*MKNK1*-2) and Cas9CTL cells using default settings. Results were then filtered on the basis of fold change (greater than 2 in either direction) and adjusted *P* value (less than 0.05). *P* values were calculated using the Wald test with false discovery rate (FDR)/Benjamini-Hochberg multiple comparison test. PCA for gene expression data was performed through the factoextra R package. One Cas9CTL technical replicate was found to be an outlier and thus removed from the dataset. Functional enrichment analyses were performed on preranked fold change data using GSEA software (Broad Institute, version 4.1.0). GSEAPreranked was run using default settings against the KEGG molecular signature database on the "Mouse Gene Symbol Remapping Human Orthologs MSigDB.v.2023.2.Hs.chip" platform.

Preparation of cell lines for proteome analysis

Quadruplicates of 4T1 Cas9CTL and sg-*MKNK1* cell lines were lysed by the addition of 100 μl of lysis buffer containing 5% SDS in 100 mM tris (pH 8.5) and heating the samples (95°C) for 10 min. Samples were consequently subjected to probe based ultrasonication (Thermo Fisher Scientific Sonic Dismembrator) and clarified by centrifugation at 21,000*g* for 5 min. Five percent of the resulting extract was reserved for the determination of protein concentration using bicinchonic acid assay (Thermo Fisher Scientific/Pierce). The remainder of the cell lysates were reduced in 20 mM tris(2-carboxyethyl)phosphine for 30 min at 60°C and alkylated in 25 mM iodoacetamide for 30 min in the dark at room temperature. Fifty micrograms of protein was proteolytically digested with trypsin (Promega, sequencing grade) overnight at 37°C using S-Trap microcartridges (ProtiFi). Peptides were eluted from S-Trap microcartridges sequentially with 50 mM ammonium bicarbonate, 0.2% formic acid, and 50% acetonitrile respectively. Peptide-containing eluates were frozen at −80°C and lyophilized to dryness using a vacuum centrifuge (Labconco). Peptide samples were reconstituted in 0.1% formic acid to a final concentration of 150 ng/μl.

Liquid chromatography–MS/MS data acquisition and analysis

An equivalent of 1 μg of protein was analyzed by nanoflow liquid chromatography–MS/MS using an Easy-nLC 1200 system coupled to a Q Exactive Plus (both Thermo Fisher Scientific). Samples were first loaded onto a precolumn (Acclaim PepMap 100 C18, 3 μm, 75 μm in internal diameter × 2 cm in length; Thermo Fisher Scientific) for online desalting and then separated using a 100-min gradient with an Acclaim PepMap 100 C18 analytical column (2-μm particle, 75 μm in ID × 250 mm; Thermo Fisher Scientific) using water with 0.1% formic acid (mobile phase A) and 84% acetonitrile with 0.1% formic acid (mobile phase B) at 300 nl/min from 3 to 40% B. MS acquisition was conducted in data-dependent acquisition mode on

the basis of the top 15 most intense precursor ions (+2 to +4 charge state). Full MS scans were acquired at 70,000 resolution from 350 to 1500 mass/charge ratio [automatic gain control (AGC), 1×10^6; 50-ms maximum injection time], and MS2 spectra were collected at 17.5K resolution (AGC, 2×10^4; 64-ms maximum injection time) using a normalized collision energy of 28. Dynamic exclusion was set to 40 s. Acquired MS/MS data were analyzed using Proteome Discoverer version 2.5 (Thermo Fisher Scientific). Database searching was conducted using the Sequest HT node, using a reference mouse proteome FASTA file containing only reviewed canonical sequences downloaded from UniProt (downloaded 28 February 2019). Label-free quantitation was conducted using the Minora feature detection node. Proteins were quantified on the basis of unique peptides and scaled on the basis of total peptide abundance, and missing values were imputed using the low abundance resampling method. Protein expression ratios were calculated on the basis of protein abundance, and *P* values were calculated using analysis of variance (ANOVA) (individual proteins) within Proteome Discoverer version 2.5. Only proteins quantified with at least one protein unique peptide in three of four biological replicates from at least one sample group were retained. Statistical significance of differentially expressed proteins was based on a two-sigma fold-change cutoff (effectively twofold change), as well as having an FDR-adjusted *P* value of less than 0.05. PCA for gene expression data was performed through the factoextra R package. Statistically differentially expressed proteins were used an input for canonical pathway enrichment analysis using Ingenuity Pathway Analysis software under default settings (QIAGEN).

Metabolomics

For each biological replicate, 4T1 Cas9CTL and sg-*MKNK1* cells were seeded at 62,500 cells per well in technical triplicate in a six-well tissue culture treated plate (Corning) and cultured in 4T1 complete medium (defined above). The following day, cells were examined, and medium was aspirated, replaced with fresh medium, and incubated for another 20 hours. Next, medium for U-[^{13}C]-glucose (Cambridge Isotopes) tracing was prepared using a base medium of 1× DMEM (Wisent, #319-062) subsequently supplemented with sodium pyruvate, glutamine, Hepes, and sodium bicarbonate to concentrations equivalent to 4T1 complete medium. Next, a 5× (125 mM) solution of U-[^{13}C]-glucose was prepared by dissolving U-[^{13}C]-glucose in the supplemented 1× DMEM. 4T1 complete medium was then aspirated from all wells and replaced with 2 ml of supplemented 1× DMEM, while 0.5 ml of 5× U-[^{13}C]-glucose was added overtop, giving a final concentration of 25 mM, and incubated (or traced) in 5% CO_2 at 37°C for 4 hours. Two wells of unlabeled controls were seeded for each cell line, which contained 2 ml of supplemented 1× DMEM and 0.5 ml of 5× ^{12}C-glucose at a final concentration of 25 mM and incubated as above for 4 hours. In addition, to normalize downstream metabolomic intensity values to cell number, three wells per cell line were seeded in 4T1 complete medium and counted at the experimental end point. To prepare the cells for metabolomic profiling, after 4 hours of incubation, plates were immediately placed on ice, and medium was aspirated. Next, wells were washed twice with 1 ml of 0.9% saline. Following saline aspiration, plates were placed over dry ice for 5 min, wrapped in aluminum foil, and immediately placed in −80°C. Cells were lysed and processed using the stable isotope labeling and metabolomics method published in Kaymak *et al.* (*44*).

Seahorse bioenergetic profiling

Before bioenergetic profiling using the Seahorse Mito Stress Test Kit (Agilent Technologies), 4T1 Cas9CTL and sg-*MKNK1* cells were seeded at 5000 cells per well in a 96-well Seahorse XFe96 FluxPak plate (Agilent Technologies) and incubated with 80 μl of DMEM (see conditions above) for 24 hours in 5% CO_2 at 37°C incubator until ~70% confluence was reached. In addition, 24 hours before bioenergetic profiling, the Seahorse Flux Assay Kit was calibrated with 200 μl of Milli-Q water (Millipore) and left in a non-CO_2, 37°C incubator for 24 hours. The following day, seeded cells were examined for appropriate confluence, and 80 μl DMEM culture medium was gently removed using a multichannel pipette and replaced with 140 μl of Seahorse XF assay medium: Seahorse XF DMEM base medium (Agilent Technologies), supplemented with 1 mM sodium pyruvate, 2 mM glutamine, and 10 mM glucose (final concentrations) (pH 7.4) at 37°C. In addition, water was removed from the flux assay kit and replaced with Seahorse XF calibrant solution (Agilent Technologies) and incubated at 37°C (non-CO_2) for 2 to 3 hours before conducting bioenergetic profiling. During the 2- to 3-hour incubation, Mito Stress Test Kit drugs—oligomycin, carbonyl cyanide *p*-trifluoromethoxyphenylhydrazone (FCCP), rotenone/antimycin A, and monensin—were dissolved in Seahorse XF assay medium to working concentrations of 16, 9, 5, and 220 μM, respectively. Next, 20 μl of each drug was pipetted into injection ports A, B, C, and D, respectively. Final drug concentrations of oligomycin, FCCP, rotenone/antimycin A, and monensin were 2, 1, 0.5, and 20.1 μM, respectively. Following the 2- to 3-hour incubation of the extracellular flux assay kit, probes were calibrated in the Seahorse Bioanalyzer. After, the flux assay kit was replaced with the 96-well plate containing Cas9CTL and MNK KO cells, while the drugs within ports remained in the machine. Oligomycin, FCCP, rotenone/antimycin A, and monensin were automatically injected overtop cells at 20, 40, 60, and 80 min, respectively. OCR and ECAR were both measured. OCR and ECAR values were normalized to cell number based on crystal violet staining and absorption at 595 nm following solubilization.

Measurement of ATP levels

Relative ATP levels were assessed using the Incucyte CytoATP Lentivirus Reagent Kit (Sartorius, #4772) according to kit instructions. Data were acquired using an Incucyte SX5 Live-Cell Analysis System configured with an SX5 Metabolism Optical Module (Sartorius, #4820). Briefly, 4T1 cells (Cas9CTL and sg-*MKNK1*) were transduced with CytoATP, and CytoATP nonbinding control lentivirus and stably expressing populations were derived via puromycin selection. Selected cells were then seeded in 96-well plates at a density of 2000 cells per well in 4T1 medium with a glucose concentration of 10 mM (low glucose). The following day, cells were treated with oligomycin and placed into the Incucyte SX5 for immediate scanning. Images were subsequently acquired every 30 min for 24 hours in total and analyzed using built-in software. Corrected ATP ratios were calculated by normalizing against CytoATP nonbinding controls and are expressed relative to Cas9CTL at baseline.

Cell assessment by flow cytometry

4T1 cells (Cas9CTL and sg-*MKNK1*) were trypsinized, centrifuged at 300*g* for 5 min, and washed in PBS. For mitochondrial assays, 1×10^5 cells were stained with 1 μM MitoSOX mitochondrial superoxide indicator (Invitrogen, #M36008) or 200 nM MitoTracker

CMXRos (Invitrogen, #M7512) according to the manufacturer's directions. For stemness assays, 2×10^5 cells were stained with fluorescently tagged antibodies that recognize CD44 and CD24 for 30 min on ice. Antibody information is listed in table S1. After staining, cells were washed in PBS, and fluorescence was assessed on an LSRFortessa (BD Biosciences).

ALDEFLUOR assay

ALDH activity in 4T1 cells (Cas9CTL and sg-*MKNK1*) was measured according to ALDEFLUOR kit instructions (STEMCELL Technologies, #01700). Briefly, 1×10^6 cells were suspended in the provided buffer and incubated with 1.5 μM BODIPY-aminoacetaldehyde for 30 min at 37°C. Using this protocol, ALDH activity is proportional to cellular fluorescence, as measured using an LSRFortessa (BD Biosciences). Background fluorescence was accounted for by treating cells with 15 μM diethylaminobenzaldehyde, a selective inhibitor of ALDH (negative control). Data were analyzed using FlowJo version 10.7.1.

Analysis of publicly available TCGA patient data

The TCGA Breast Invasive Carcinoma PanCancer Atlas database was accessed through cBioPortal. Analysis was limited to only patients for whom MNK1 protein expression *z*-score, and overall survival data were available ($n = 102$). Full protein expression data and matching clinical correlates were downloaded for these patients only. Expression heatmaps were generated using Prism 9. ssGSEA was subsequently performed according to methodology described in Barbie *et al.* (*78*), using KEGG Glycolysis_Gluconeogenesis, Oxidative_Phosphorylation, Citric_Cycle_TCA_Cycle, Wnt_Signaling, and Hedgehog_Signaling gene sets. Analysis was performed on the GenePattern cloud–based public server, using the "ssGSEA" module (v10.1.0). Input data (protein expression *z*-scores from MS by the National Cancer Institute's Clinical Proteomic Tumor Analysis Consortium) for relevant patients were downloaded from cBioPortal. Gene set database files were downloaded from the GSEA MSigDB. Default settings were used for all other analysis parameters. Pearson rank-order calculations were performed to correlate MNK1 protein expression with individual proteins of interest and ssGSEA enrichment scores. Analysis of overall survival data was performed on the highest and lowest quartile of patients when ranked by MNK1 protein expression.

Histology and IHC

Following FFPE processing, all samples were sectioned at 4 μm in thickness according to staining requirements. Tumor-bearing livers were step-sectioned (two steps, 200 μm between steps) for subsequent staining with H&E as previously described (*17*). IHC stainings were performed on primary tumor and tumor-bearing liver tissues. Slides were deparaffinized, rehydrated, and subjected to heat-induced antigen retrieval. Endogenous peroxidase activity was quenched for 15 min in 10% hydrogen peroxide, and tissues were blocked in 10% donkey serum (Jackson ImmunoResearch, #017-000-121). Tissues were then stained with antibodies specific to MNK1 (tumors; 1:50 dilution) or phospho-eIF4E (tumor-bearing livers; 1:50 dilution). Stainings were visualized using ImmPACT DAB (3,3′-diaminobenzidine) (Vector Laboratories, #SK-4105) and counterstained with Harris-modified hematoxylin (EMD Millipore, #638A-85). All stained slides were imaged using a Zeiss AxioScan.Z1 slide scanner and analyzed using QuPath version 0.2.3. See table S1 for antibody details.

Immunoblotting

Immunoblotting was performed as previously detailed (*15*). Briefly, protein lysates were isolated from cell pellets using radioimmunoprecipitation assay buffer [150 mM tris-HCl (pH 7), 150 mM NaCl, 1% NP-40, 1% sodium deoxycholate, and 0.1% SDS]. Protein concentrations were measured by Bradford reagent assay (Bio-Rad), separated on a 10% SDS-polyacrylamide gel electrophoresis gel, and transferred to nitrocellulose membranes. Membranes were blocked in 5% nonfat milk and incubated in primary antibody dilutions overnight at 4°C. The following day, membranes were incubated with secondary antibody at room temperature for 1 hour. Membranes were then revealed using ECL Prime Western Blotting Detection Reagent (Amersham) and Ultra-High Contrast Western Blotting Film. Antibody information is listed in table S1. Immunoblot densitometry analysis was performed for all proteins, normalizing against a β-actin loading control, and is displayed in fig. S9.

Cell proliferation growth curves

4T1 cells (Cas9CTL and sg-*MKNK1*) were serum-starved for 16 hours before seeding in 96-well plates at a density of 1000 cells per well. At 24-hour intervals, up to 96 hours after seeding, cells were fixed in 4% PFA for 15 min at room temperatures and stored in 0.4% PFA. Fixed cells were stained with 0.5% crystal violet at end point for 30 min at room temperature. The following day, crystal violet was dissolved in 10% acetic acid, and absorbance was measured at 590 nm using a plate reader. Cell proliferation over time was calculated relative to a standard curve of known cell numbers.

Statistics

Prism 9 software (GraphPad) was used to perform statistical testing. Details of the statistical testing performed for all relevant figure panels can be found in in figure legends. *P* values for the differences of means between groups were calculated using unpaired *t* tests, one-way ANOVA, two-way ANOVA, and Pearson rank-order correlations, with multiple comparison tests as appropriate. *P* values less than 0.05 were considered statistically significant.

Supplementary Materials

This PDF file includes:

Figs. S1 to S9
Table S1

REFERENCES AND NOTES

1. F. Bray, J. Ferlay, I. Soerjomataram, R. L. Siegel, L. A. Torre, A. Jemal, Global cancer statistics 2018: GLOBOCAN estimates of incidence and mortality worldwide for 36 cancers in 185 countries. *CA Cancer J. Clin.* **68**, 394–424 (2018).
2. American Cancer Society, *Cancer Facts & Figures 2020* (American Cancer Society, 2020).
3. H.-Y. Zhao, Y. Gong, F.-G. Ye, H. Ling, X. Hu, Incidence and prognostic factors of patients with synchronous liver metastases upon initial diagnosis of breast cancer: A population-based study. *Cancer Manag. Res.* **10**, 5937–5950 (2018).
4. J. Chu, M. Cargnello, I. Topisirovic, J. Pelletier, Translation initiation factors: Reprogramming protein synthesis in cancer. *Trends Cell Biol.* **26**, 918–933 (2016).
5. A. Lazaris-Karatzas, K. S. Montine, N. Sonenberg, Malignant transformation by a eukaryotic initiation factor subunit that binds to mRNA 5′ cap. *Nature* **345**, 544–547 (1990).
6. A. J. Waskiewicz, A. Flynn, C. G. Proud, J. A. Cooper, Mitogen-activated protein kinases activate the serine/threonine kinases Mnk1 and Mnk2. *EMBO J.* **16**, 1909–1920 (1997).
7. A. J. Waskiewicz, J. C. Johnson, B. Penn, M. Mahalingam, S. R. Kimball, J. A. Cooper, Phosphorylation of the cap-binding protein eukaryotic translation initiation factor 4E by protein kinase Mnk1 in vivo. *Mol. Cell. Biol.* **19**, 1871–1880 (1999).

8. I. Topisirovic, M. Ruiz-Gutierrez, K. L. B. Borden, Phosphorylation of the eukaryotic translation initiation factor eIF4E contributes to its transformation and mRNA transport activities. *Cancer Res.* **64**, 8639–8642 (2004).
9. L. Furic, L. Rong, O. Larsson, I. H. Koumakpayi, K. Yoshida, A. Brueschke, E. Petroulakis, N. Robichaud, M. Pollak, L. A. Gaboury, P. P. Pandolfi, F. Saad, N. Sonenberg, eIF4E phosphorylation promotes tumorigenesis and is associated with prostate cancer progression. *Proc. Natl. Acad. Sci. U.S.A.* **107**, 14134–14139 (2010).
10. N. Robichaud, S. V. del Rincon, B. Huor, T. Alain, L. A. Petruccelli, J. Hearnden, C. Goncalves, S. Grotegut, C. H. Spruck, L. Furic, O. Larsson, W. J. Muller, W. H. Miller, N. Sonenberg, Phosphorylation of eIF4E promotes EMT and metastasis via translational control of SNAIL and MMP-3. *Oncogene* **34**, 2032–2042 (2015).
11. N. Robichaud, B. E. Hsu, R. Istomine, F. Alvarez, J. Blagih, E. H. Ma, S. V. Morales, D. L. Dai, G. Li, M. Souleimanova, Q. Guo, S. V. Del Rincon, W. H. Miller Jr., S. R. Y. Cajal, M. Park, R. G. Jones, C. A. Piccirillo, P. M. Siegel, N. Sonenberg, Translational control in the tumor microenvironment promotes lung metastasis: Phosphorylation of eIF4E in neutrophils. *Proc. Natl. Acad. Sci. U.S.A.* **115**, E2202–E2209 (2018).
12. Q. Guo, M. Bartish, C. Gonçalves, F. Huang, J. Smith-Voudouris, S. S. Krisna, S. E. J. Preston, A. Emond, V. Z. Li, C. U. Duerr, Y. Gui, A. Cleret-Buhot, P. Thebault, H. Lefrère, L. Lenaerts, D. Plourde, J. Su, B. C. Mindt, S. A. Hewgill, T. Cotechini, C. C. T. Hindmarch, W. Yang, E. Khoury, Y. Zhan, V. Narykina, Y. Wei, G. Floris, M. Basik, F. Amant, D. F. Quail, R. Lapointe, J. H. Fritz, S. V. Del Rincon, W. H. J. Miller, The MNK1/2-eIF4E axis supports immune suppression and metastasis in postpartum breast cancer. *Cancer Res.* **81**, 3876–3889 (2021).
13. F. Huang, C. Gonçalves, M. Bartish, J. Rémy-Sarrazin, M. E. Issa, B. Cordeiro, Q. Guo, A. Emond, M. Attias, W. Yang, D. Plourde, J. Su, M. G. Gimeno, Y. Zhan, A. Galán, T. Rzymski, M. Mazan, M. Masiejczyk, J. Faber, E. Khoury, A. Benoit, N. Gagnon, D. Dankort, F. Journe, G. E. Ghanem, C. M. Krawczyk, H. U. Saragovi, C. A. Piccirillo, N. Sonenberg, I. Topisirovic, C. E. Rudd, W. H. Miller Jr., S. V. del Rincón, Inhibiting the MNK1/2-eIF4E axis impairs melanoma phenotype switching and potentiates antitumor immune responses. *J. Clin. Invest.* **131**, e181575 (2021).
14. M. Bartish, D. Tong, Y. Pan, M. Wallerius, H. Liu, J. Ristau, S. de Souza Ferreira, T. Wallmann, V. van Hoef, L. Masvidal, T. Kerzel, A.-L. Joly, C. Goncalves, S. E. J. Preston, T. Ebrahimian, C. Seitz, J. Bergh, K. Pietras, S. Lehoux, L. Naldini, J. Andersson, M. L. Squadrito, S. V. Del Rincón, O. Larsson, C. Rolny, MNK2 governs the macrophage antiinflammatory phenotype. *Proc. Natl. Acad. Sci. U.S.A.* **117**, 27556–27565 (2020).
15. S. E. J. Preston, M. Bartish, V. R. Richard, A. Aghigh, C. Gonçalves, J. Smith-Voudouris, F. Huang, P. Thébault, A. Cleret-Buhot, R. Lapointe, F. Légaré, L.-M. Postovit, R. P. Zahedi, C. H. Borchers, W. H. J. Miller, S. V. Del Rincón, Phosphorylation of eIF4E in the stroma drives the production and spatial organisation of collagen type I in the mammary gland. *Matrix Biol.* **111**, 264–288 (2022).
16. J. H. Carter, J. A. Deddens, N. R. I. V. Spaulding, D. Lucas, B. M. Colligan, T. G. Lewis, E. Hawkins, J. Jones, J. O. Pemberton, L. E. Douglass, J. R. Graff, Phosphorylation of eIF4E serine 209 is associated with tumour progression and reduced survival in malignant melanoma. *Br. J. Cancer* **114**, 444–453 (2016).
17. Q. Guo, V. Z. Li, J. N. Nichol, F. Huang, W. Yang, S. E. J. Preston, Z. Talat, H. Lefrère, H. Yu, G. Zhang, M. Basik, C. Gonçalves, Y. Zhan, D. Plourde, J. Su, J. Torres, M. Marques, S. Al Habyan, K. Bijian, F. Amant, M. Witcher, F. Behbod, L. McCaffrey, M. Alaoui-Jamali, N. V. Giannakopoulos, M. Brackstone, L.-M. Postovit, S. V. Del Rincón, W. H. Miller Jr., MNK1/NODAL signaling promotes invasive progression of breast ductal carcinoma in situ. *Cancer Res.* **79**, 1646–1657 (2019).
18. S. Ricardo, A. F. Vieira, R. Gerhard, D. Leitão, R. Pinto, J. F. Cameselle-Teijeiro, F. Milanezi, F. Schmitt, J. Paredes, Breast cancer stem cell markers CD44, CD24 and ALDH1: Expression distribution within intrinsic molecular subtype. *J. Clin. Pathol.* **64**, 937–946 (2011).
19. I. Rabinovich, A. P. M. Sebastião, R. S. Lima, C. D. A. Urban, E. S. Junior, K. F. Anselmi, S. Elifio-Esposito, L. De Noronha, A. N. Moreno-Amaral, Cancer stem cell markers ALDH1 and $CD44^{+}/CD24^{-}$ phenotype and their prognosis impact in invasive ductal carcinoma. *Eur. J. Histochem.* **62**, (2018).
20. A. Albini, A. Bruno, C. Gallo, G. Pajardi, D. M. Noonan, K. Dallaglio, Cancer stem cells and the tumor microenvironment: Interplay in tumor heterogeneity. *Connect. Tissue Res.* **56**, 414–425 (2015).
21. H. Clevers, The cancer stem cell: Premises, promises and challenges. *Nat. Med.* **17**, 313–319 (2011).
22. C.-Y. Lin, K. Q. Barry-Holson, K. H. Allison, Breast cancer stem cells: Are we ready to go from bench to bedside? *Histopathology* **68**, 119–137 (2016).
23. X. Zhang, K. Powell, L. Li, Breast cancer stem cells: Biomarkers, identification and isolation methods, regulating mechanisms, cellular origin, and beyond. *Cancers* **12**, 3765 (2020).
24. P. Sancho, D. Barneda, C. Heeschen, Hallmarks of cancer stem cell metabolism. *Br. J. Cancer* **114**, 1305–1312 (2016).
25. S. Bartlome, C. C. Berry, Recent insights into the effects of metabolism on breast cancer cell dormancy. *Br. J. Cancer* **127**, 1385–1393 (2022).
26. K. Chen, C. Zhang, S. Ling, R. Wei, J. Wang, X. Xu, The metabolic flexibility of quiescent CSC: Implications for chemotherapy resistance. *Cell Death Dis.* **12**, 835 (2021).
27. U. P. Yadav, T. Singh, P. Kumar, P. Sharma, H. Kaur, S. Sharma, S. Singh, S. Kumar, K. Mehta, Metabolic adaptations in cancer stem cells. *Front. Oncol.* **10**, 1010 (2020).
28. S. Lim, T. Y. Saw, M. Zhang, M. R. Janes, K. Nacro, J. Hill, A. Q. Lim, C.-T. Chang, D. A. Fruman, D. A. Rizzieri, S. Y. Tan, H. Fan, C. T. H. Chuah, S. T. Ong, Targeting of the MNK-eIF4E axis in blast crisis chronic myeloid leukemia inhibits leukemia stem cell function. *Proc. Natl. Acad. Sci. U.S.A.* **110**, E2298–E2307 (2013).
29. J. B. Bell, F. D. Eckerdt, K. Alley, L. P. Magnusson, H. Hussain, Y. Bi, A. D. Arslan, J. Clymer, A. A. Alvarez, S. Goldman, S.-Y. Cheng, I. Nakano, C. Horbinski, R. V. Davuluri, C. D. James, L. C. Platanias, MNK inhibition disrupts mesenchymal glioma stem cells and prolongs survival in a mouse model of glioblastoma. *Mol. Cancer Res.* **14**, 984–993 (2016).
30. F. Dupuy, S. Tabariès, S. Andrzejewski, Z. Dong, J. Blagih, M. G. Annis, A. Omeroglu, D. Gao, S. Leung, E. Amir, M. Clemons, A. Aguilar-Mahecha, M. Basik, E. E. Vincent, J. St-Pierre, R. G. Jones, P. M. Siegel, PDK1-dependent metabolic reprogramming dictates metastatic potential in breast cancer. *Cell Metab.* **22**, 577–589 (2015).
31. R. T. Davis, K. Blake, D. Ma, M. B. I. Gabra, G. A. Hernandez, A. T. Phung, Y. Yang, D. Maurer, A. E. Y. T. Lefebvre, H. Alshetaiwi, Z. Xiao, J. Liu, J. W. Locasale, M. A. Digman, E. Mjolsness, M. Kong, Z. Werb, D. A. Lawson, Transcriptional diversity and bioenergetic shift in human breast cancer metastasis revealed by single-cell RNA sequencing. *Nat. Cell Biol.* **22**, 310–320 (2020).
32. I. Elia, M. Rossi, S. Stegen, D. Broekaert, G. Doglioni, M. van Gorsel, R. Boon, C. Escalona-Noguero, S. Torrekens, C. Verfaillie, E. Verbeken, G. Carmeliet, S.-M. Fendt, Breast cancer cells rely on environmental pyruvate to shape the metastatic niche. *Nature* **568**, 117–121 (2019).
33. G. B. Ferraro, A. Ali, A. Luengo, D. P. Kodack, A. Deik, K. L. Abbott, D. Bezwada, L. Blanc, B. Prideaux, X. Jin, J. M. Posada, J. Chen, C. R. Chin, Z. Amoozgar, R. Ferreira, I. X. Chen, K. Naxerova, C. Ng, A. M. Westermark, M. Duquette, S. Roberge, N. I. Lindeman, C. A. Lyssiotis, J. Nielsen, D. E. Housman, D. G. Duda, E. Brachtel, T. R. Golub, L. C. Cantley, J. M. Asara, S. M. Davidson, D. Fukumura, V. A. Dartois, C. B. Clish, R. K. Jain, M. G. Vander Heiden, Fatty acid synthesis is required for breast cancer brain metastasis. *Nat. Cancer* **2**, 414–428 (2021).
34. S. A. Mani, W. Guo, M.-J. Liao, E. N. Eaton, A. Ayyanan, A. Y. Zhou, M. Brooks, F. Reinhard, C. C. Zhang, M. Shipitsin, L. L. Campbell, K. Polyak, C. Brisken, J. Yang, R. A. Weinberg, The epithelial-mesenchymal transition generates cells with properties of stem cells. *Cell* **133**, 704–715 (2008).
35. C. Ginestier, M. H. Hur, E. Charafe-Jauffret, F. Monville, J. Dutcher, M. Brown, J. Jacquemier, P. Viens, C. G. Kleer, S. Liu, A. Schott, D. Hayes, D. Birnbaum, M. S. Wicha, G. Dontu, ALDH1 is a marker of normal and malignant human mammary stem cells and a predictor of poor clinical outcome. *Cell Stem Cell* **1**, 555–567 (2007).
36. M. G. V. Heiden, L. C. Cantley, C. B. Thompson, Understanding the Warburg effect: The metabolic requirements of cell proliferation. *Science* **324**, 1029–1033 (2009).
37. C. D. L. Folmes, T. J. Nelson, A. Martinez-Fernandez, D. K. Arrell, J. Z. Lindor, P. P. Dzeja, Y. Ikeda, C. Perez-Terzic, A. Terzic, Somatic oxidative bioenergetics transitions into pluripotency-dependent glycolysis to facilitate nuclear reprogramming. *Cell Metab.* **14**, 264–271 (2011).
38. C. Dong, T. Yuan, Y. Wu, Y. Wang, T. W. M. Fan, S. Miriyala, Y. Lin, J. Yao, J. Shi, T. Kang, P. Lorkiewicz, D. St Clair, M.-C. Hung, B. M. Evers, B. P. Zhou, Loss of FBP1 by Snail-mediated repression provides metabolic advantages in basal-like breast cancer. *Cancer Cell* **23**, 316–331 (2013).
39. C. A. Yuen, S. Asuthkar, M. R. Guda, A. J. Tsung, K. K. Velpula, Cancer stem cell molecular reprogramming of the Warburg effect in glioblastomas: A new target gleaned from an old concept. *CNS Oncol.* **5**, 101–108 (2016).
40. A. Le, C. R. Cooper, A. M. Gouw, R. Dinavahi, A. Maitra, L. M. Deck, R. E. Royer, D. L. Vander Jagt, G. L. Semenza, C. V. Dang, Inhibition of lactate dehydrogenase A induces oxidative stress and inhibits tumor progression. *Proc. Natl. Acad. Sci. U.S.A.* **107**, 2037–2042 (2010).
41. A. Rizwan, I. Serganova, R. Khanin, H. Karabeber, X. Ni, S. Thakur, K. L. Zakian, R. Blasberg, J. A. Koutcher, Relationships between LDH-A, lactate, and metastases in 4T1 breast tumors. *Clin. Cancer Res.* **19**, 5158–5169 (2013).
42. W. Li, T. Tanikawa, I. Kryczek, H. Xia, G. Li, K. Wu, S. Wei, L. Zhao, L. Vatan, B. Wen, P. Shu, D. Sun, C. Kleer, M. Wicha, M. Sabel, K. Tao, G. Wang, W. Zou, Aerobic glycolysis controls myeloid-derived suppressor cells and tumor immunity via a specific CEBPB isoform in triple-negative breast cancer. *Cell Metab.* **28**, 87–103.e6 (2018).
43. S. R. Hingorani, L. Wang, A. S. Multani, C. Combs, T. B. Deramaudt, R. H. Hruban, A. K. Rustgi, S. Chang, D. A. Tuveson, *Trp53R172H* and *KrasG12D* cooperate to promote chromosomal instability and widely metastatic pancreatic ductal adenocarcinoma in mice. *Cancer Cell* **7**, 469–483 (2005).
44. I. Kaymak, K. M. Luda, L. R. Duimstra, E. H. Ma, J. Longo, M. S. Dahabieh, B. Faubert, B. M. Oswald, M. J. Watson, S. M. Kitchen-Goosen, L. M. DeCamp, S. E. Compton, Z. Fu, R. J. DeBerardinis, K. S. Williams, R. D. Sheldon, R. G. Jones, Carbon source availability drives nutrient utilization in $CD8^{+}$ T cells. *Cell Metab.* **34**, 1298–1311.e6 (2022).
45. R. J. DeBerardinis, A. Mancuso, E. Daikhin, I. Nissim, M. Yudkoff, S. Wehrli, C. B. Thompson, Beyond aerobic glycolysis: Transformed cells can engage in glutamine metabolism that

exceeds the requirement for protein and nucleotide synthesis. *Proc. Natl. Acad. Sci. U.S.A.* **104**, 19345–19350 (2007).
46. F. Pacifico, A. Leonardi, E. Crescenzi, Glutamine metabolism in cancer stem cells: A complex liaison in the tumor microenvironment. *Int. J. Mol. Sci.* **24**, 2337 (2023).
47. J. Li, Z.-Q. Hu, S.-Y. Yu, L. Mao, Z.-J. Zhou, P.-C. Wang, Y. Gong, S. Su, J. Zhou, J. Fan, S.-L. Zhou, X.-W. Huang, CircRPN2 inhibits aerobic glycolysis and metastasis in hepatocellular carcinoma. *Cancer Res.* **82**, 1055–1069 (2022).
48. S. Zhao, B. Guan, Y. Mi, D. Shi, P. Wei, Y. Gu, S. Cai, Y. Xu, X. Li, D. Yan, M. Huang, D. Li, LncRNA MIR17HG promotes colorectal cancer liver metastasis by mediating a glycolysis-associated positive feedback circuit. *Oncogene* **40**, 4709–4724 (2021).
49. R. K. Nimmakayala, F. Leon, S. Rachagani, S. Rauth, P. Nallasamy, S. Marimuthu, G. K. Shailendra, Y. S. Chhonker, S. Chugh, R. Chirravuri, R. Gupta, K. Mallya, D. R. Prajapati, S. M. Lele, T. C. Caffrey, J. L. Grem, P. M. Grandgenett, M. A. Hollingsworth, D. J. Murry, S. K. Batra, M. P. Ponnusamy, Metabolic programming of distinct cancer stem cells promotes metastasis of pancreatic ductal adenocarcinoma. *Oncogene* **40**, 215–231 (2021).
50. Y. Zhan, J. Guo, W. Yang, C. Goncalves, T. Rzymski, A. Dreas, E. Żyłkiewicz, M. Mikulski, K. Brzózka, A. Golas, Y. Kong, M. Ma, F. Huang, B. Huor, Q. Guo, S. D. da Silva, J. Torres, Y. Cai, I. Topisirovic, J. Su, K. Bijian, M. A. Alaoui-Jamali, S. Huang, F. Journe, G. E. Ghanem, W. H. Miller Jr., S. V. Del Rincón, MNK1/2 inhibition limits oncogenicity and metastasis of KIT-mutant melanoma. *J. Clin. Invest.* **127**, 4179–4192 (2017).
51. W. Yang, E. Khoury, Q. Guo, S. A. Prabhu, A. Emond, F. Huang, C. Gonçalves, Y. Zhan, D. Plourde, J. N. Nichol, M. S. Dahabieh, W. H. Miller Jr., S. V. del Rincón, MNK1 signaling induces an ANGPTL4-mediated gene signature to drive melanoma progression. *Oncogene* **39**, 3650–3665 (2020).
52. A. Tsuji, T. Akao, T. Masuya, M. Murai, H. Miyoshi, IACS-010759, a potent inhibitor of glycolysis-deficient hypoxic tumor cells, inhibits mitochondrial respiratory complex I through a unique mechanism. *J. Biol. Chem.* **295**, 7481–7491 (2020).
53. T. Schild, V. Low, J. Blenis, A. P. Gomes, Unique metabolic adaptations dictate distal organ-specific metastatic colonization. *Cancer Cell* **33**, 347–354 (2018).
54. C. Lehuédé, F. Dupuy, R. Rabinovitch, R. G. Jones, P. M. Siegel, Metabolic plasticity as a determinant of tumor growth and metastasis. *Cancer Res.* **76**, 5201–5208 (2016).
55. J. Hu, G. Li, P. Zhang, X. Zhuang, G. Hu, A $CD44v^+$ subpopulation of breast cancer stem-like cells with enhanced lung metastasis capacity. *Cell Death Dis.* **8**, e2679 (2017).
56. W. Gao, L. Chen, Z. Ma, Z. Du, Z. Zhao, Z. Hu, Q. Li, Isolation and phenotypic characterization of colorectal cancer stem cells with organ-specific metastatic potential. *Gastroenterology* **145**, 636–46.e5 (2013).
57. H. Ying, A. C. Kimmelman, C. A. Lyssiotis, S. Hua, G. C. Chu, E. Fletcher-Sananikone, J. W. Locasale, J. Son, H. Zhang, J. L. Coloff, H. Yan, W. Wang, S. Chen, A. Viale, H. Zheng, J. Paik, C. Lim, A. R. Guimaraes, E. S. Martin, J. Chang, A. F. Hezel, S. R. Perry, J. Hu, B. Gan, Y. Xiao, J. M. Asara, R. Weissleder, Y. A. Wang, L. Chin, L. C. Cantley, R. A. DePinho, Oncogenic Kras maintains pancreatic tumors through regulation of anabolic glucose metabolism. *Cell* **149**, 656–670 (2012).
58. A. Viale, P. Pettazzoni, C. A. Lyssiotis, H. Ying, N. Sánchez, M. Marchesini, A. Carugo, T. Green, S. Seth, V. Giuliani, M. Kost-Alimova, F. Muller, S. Colla, L. Nezi, G. Genovese, A. K. Deem, A. Kapoor, W. Yao, E. Brunetto, Y. Kang, M. Yuan, J. M. Asara, Y. A. Wang, T. P. Heffernan, A. C. Kimmelman, H. Wang, J. B. Fleming, L. C. Cantley, R. A. DePinho, G. F. Draetta, Oncogene ablation-resistant pancreatic cancer cells depend on mitochondrial function. *Nature* **514**, 628–632 (2014).
59. L. Y. Sandeman, W. X. Kang, X. Wang, K. B. Jensen, D. Wong, T. Bo, L. Gao, J. Zhao, C. D. Byrne, A. J. Page, C. G. Proud, Disabling MNK protein kinases promotes oxidative metabolism and protects against diet-induced obesity. *Mol. Metab.* **42**, 101054 (2020).
60. C. S. Conn, H. Yang, H. J. Tom, K. Ikeda, J. A. Oses-Prieto, H. Vu, Y. Oguri, S. Nair, R. M. Gill, S. Kajimura, R. J. DeBerardinis, A. L. Burlingame, D. Ruggero, The major cap-binding protein eIF4E regulates lipid homeostasis and diet-induced obesity. *Nat. Metab.* **3**, 244–257 (2021).
61. M. Bartish, M. J. Abraham, C. Gonçalves, O. Larsson, C. Rolny, S. V. Del Rincón, The role of eIF4F-driven mRNA translation in regulating the tumour microenvironment. *Nat. Rev. Cancer* **23**, 408–425 (2023).
62. G. Bergers, S.-M. Fendt, The metabolism of cancer cells during metastasis. *Nat. Rev. Cancer* **21**, 162–180 (2021).
63. P. J. Goodwin, B. E. Chen, K. A. Gelmon, T. J. Whelan, M. Ennis, J. Lemieux, J. A. Ligibel, D. L. Hershman, I. A. Mayer, T. J. Hobday, J. M. Bliss, P. Rastogi, M. Rabaglio-Poretti, S. D. Mukherjee, J. R. Mackey, V. G. Abramson, C. Oja, R. Wesolowski, A. M. Thompson, D. W. Rea, P. M. Stos, L. E. Shepherd, V. Stambolic, W. R. Parulekar, Effect of metformin vs placebo on invasive disease–free survival in patients with breast cancer: The MA.32 randomized clinical trial. *JAMA* **327**, 1963–1973 (2022).
64. N. F. Col, L. Ochs, V. Springmann, A. K. Aragaki, R. T. Chlebowski, Metformin and breast cancer risk: A meta-analysis and critical literature review. *Breast Cancer Res. Treat.* **135**, 639–646 (2012).
65. Z. Lv, X. Yan, L. Lu, C. Su, Y. He, Atovaquone enhances doxorubicin's efficacy via inhibiting mitochondrial respiration and STAT3 in aggressive thyroid cancer. *J. Bioenerg. Biomembr.* **50**, 263–270 (2018).
66. T. A. Yap, N. Daver, M. Mahendra, J. Zhang, C. Kamiya-Matsuoka, F. Meric-Bernstam, H. M. Kantarjian, F. Ravandi, M. E. Collins, M. E. Di Francesco, E. E. Dumbrava, S. Fu, S. Gao, J. P. Gay, S. Gera, J. Han, D. S. Hong, E. J. Jabbour, Z. Ju, D. D. Karp, A. Lodi, J. R. Molina, N. Baran, A. Naing, M. Ohanian, S. Pant, N. Pemmaraju, P. Bose, S. A. Piha-Paul, J. Rodon, C. Salguero, K. Sasaki, A. K. Singh, V. Subbiah, A. M. Tsimberidou, Q. A. Xu, M. Yilmaz, Q. Zhang, Y. Li, C. A. Bristow, M. B. Bhattacharjee, S. Tiziani, T. P. Heffernan, C. P. Vellano, P. Jones, C. J. Heijnen, A. Kavelaars, J. R. Marszalek, M. Konopleva, Complex I inhibitor of oxidative phosphorylation in advanced solid tumors and acute myeloid leukemia: Phase I trials. *Nat. Med.* **29**, 115–126 (2023).
67. M. Leibovitch, I. Topisirovic, Dysregulation of mRNA translation and energy metabolism in cancer. *Adv. Biol. Regul.* **67**, 30–39 (2018).
68. D. Mossmann, S. Park, M. N. Hall, mTOR signalling and cellular metabolism are mutual determinants in cancer. *Nat. Rev. Cancer* **18**, 744–757 (2018).
69. K. Fooks, G. Galicia-Vazquez, V. Gife, A. Schcolnik-Cabrera, Z. Nouhi, W. W. L. Poon, V. Luo, R. N. Rys, R. Aloyz, A. Orthwein, N. A. Johnson, L. Hulea, F. E. Mercier, EIF4A inhibition targets bioenergetic homeostasis in AML MOLM-14 cells in vitro and in vivo and synergizes with cytarabine and venetoclax. *J. Exp. Clin. Cancer Res.* **41**, 340 (2022).
70. M. Morita, S.-P. Gravel, V. Chénard, K. Sikström, L. Zheng, T. Alain, V. Gandin, D. Avizonis, M. Arguello, C. Zakaria, S. McLaughlan, Y. Nouet, A. Pause, M. Pollak, E. Gottlieb, O. Larsson, J. St-Pierre, I. Topisirovic, N. Sonenberg, mTORC1 controls mitochondrial activity and biogenesis through 4E-BP-dependent translational regulation. *Cell Metab.* **18**, 698–711 (2013).
71. D. Sheinboim, S. Parikh, P. Manich, I. Markus, S. Dahan, R. Parikh, E. Stubbs, G. Cohen, V. Zemser-Werner, R. E. Bell, S. A. Ruiz, R. Percik, R. Brenner, S. Leibou, H. Vaknine, G. Arad, Y. Gerber, L. Keinan-Boker, T. Shimony, L. Bikovski, N. Goldstein, K. Constantini, S. Labes, S. Mordechai, H. Doron, A. Lonescu, T. Ziv, E. Nizri, G. Choshen, H. Eldar-Finkelman, Y. Tabach, A. Helman, S. Ben-Eliyahu, N. Erez, E. Perlson, T. Geiger, D. Ben-Zvi, M. Khaled, Y. Gepner, C. Levy, An exercise-induced metabolic shield in distant organs blocks cancer progression and metastatic dissemination. *Cancer Res.* **82**, 4164–4178 (2022).
72. J. E. Merrett, J. Xie, P. J. Psaltis, C. G. Proud, MAPK-interacting kinase 2 (MNK2) regulates adipocyte metabolism independently of its catalytic activity. *Biochem. J.* **477**, 2735–2754 (2020).
73. M. Békés, D. R. Langley, C. M. Crews, PROTAC targeted protein degraders: The past is prologue. *Nat. Rev. Drug Discov.* **21**, 181–200 (2022).
74. S. Ramalingam, V. P. Ramamurthy, L. K. Gediya, F. N. Murigi, P. Purushottamachar, W. Huang, E. Y. Choi, Y. Zhang, T. S. Vasaitis, M. A. Kane, R. G. Lapidus, V. C. O. Njar, The novel Mnk1/2 degrader and apoptosis inducer VNLG-152 potently inhibits TNBC tumor growth and metastasis. *Cancers* **11**, 299 (2019).
75. G. C. Scheper, N. A. Morrice, M. Kleijn, C. G. Proud, The mitogen-activated protein kinase signal-integrating kinase Mnk2 is a eukaryotic initiation factor 4E kinase with high levels of basal activity in mammalian cells. *Mol. Cell. Biol.* **21**, 743–754 (2001).
76. J. L. Parra, M. Buxadé, C. G. Proud, Features of the catalytic domains and C termini of the MAPK signal-integrating kinases Mnk1 and Mnk2 determine their differing activities and regulatory properties. *J. Biol. Chem.* **280**, 37623–37633 (2005).
77. S. A. Prabhu, O. Moussa, C. Gonçalves, J. H. LaPierre, H. Chou, F. Huang, V. R. Richard, P. Y. M. Ferruzo, E. M. Guettler, I. Soria-Bretones, L. Kirby, N. Gagnon, J. Su, J. Silvester, S. S. Krisna, A. A. N. Rose, K. E. Sheppard, D. W. Cescon, F. A. Mallette, R. P. Zahedi, C. H. Borchers, S. V. del Rincon, W. H. Miller Jr., Inhibition of the MNK1/2–eIF4E axis augments palbociclib-mediated antitumor activity in melanoma and breast cancer. *Mol. Cancer Ther.* **22**, 192–204 (2023).
78. D. A. Barbie, P. Tamayo, J. S. Boehm, S. Y. Kim, S. E. Moody, I. F. Dunn, A. C. Schinzel, P. Sandy, E. Meylan, C. Scholl, S. Fröhling, E. M. Chan, M. L. Sos, K. Michel, C. Mermel, S. J. Silver, B. A. Weir, J. H. Reiling, Q. Sheng, P. B. Gupta, R. C. Wadlow, H. Le, S. Hoersch, B. S. Wittner, S. Ramaswamy, D. M. Livingston, D. M. Sabatini, M. Meyerson, R. K. Thomas, E. S. Lander, J. P. Mesirov, D. E. Root, D. G. Gilliland, T. Jacks, W. C. Hahn, Systematic RNA interference reveals that oncogenic KRAS-driven cancers require TBK1. *Nature* **462**, 108–112 (2009).

Acknowledgments: We wish to thank J. Huber, the IRIC Next Generation Sequencing Core Facility (Université de Montréal), the IRIC Histology Core Facility (Université de Montréal), N. Benlimame, L. Canetti, and J. Longo for technical support. We extend our gratitude to K. A. Forner and V. Michaud for expertise and assistance in developing animal models. C.H.B. is grateful for support from the Segal McGill Chair in Molecular Oncology at McGill University (Montreal, Quebec, Canada). C.H.B. is also grateful for support from the Warren Y. Soper Charitable Trust, the Alvin Segal Family Foundation of the Jewish General Hospital (Montreal, Quebec, Canada), and the Terry Fox Research Institute. **Funding:** This work was supported by Canadian Cancer Society grant #707140 (to S.V.d.R., W.H.M., C.H.B., and R.P.Z.), Canadian Institute of Health–Institute of Cancer Research/Cancer Research Society Partnership CRP 173603 (to S.V.d.R. and P.B.), Genome Canada (Genomics Technology Platform) #264PRO (to C.H.B.), Fonds de Recherche Québec Santé Doctoral Fellowship (to S.E.J.P.), Fonds de Recherche Québec Santé Doctoral Fellowship (to R.E.F.G.), Epstein Fellowship in Women's Health, McGill University (to S.E.J.P.), Canadian Institute of Health Research–Canada Graduate Scholarship, CIHR-CGS-M (to P.A.M.). **Author contributions:**

Conceptualization: S.E.J.P., M.S.D., W.H.M., S.V.d.R., C.G., and R.E.F.G. Methodology: S.E.J.P., M.S.D., P.B., W.H.M., S.V.d.R., C.G., V.R.R., C.H.B., R.E.F.G., N.G., and R.G.J. Investigation: S.E.J.P., M.S.D., T.P., E.D., V.R.R., R.E.F.G., S.P., C.L.N., M.L., and F.H. Validation: S.E.J.P., M.S.D., P.B., W.H.M., E.D., S.V.d.R., R.E.F.G., R.G.J., and F.H. Visualization: S.E.J.P., M.S.D., P.A.M., S.V.d.R., R.E.F.G., and R.G.J. Formal analysis: S.E.J.P., M.S.D., W.H.M., R.P.Z., C.G., V.R.R., R.E.F.G., and R.G.J. Software: C.G. Data curation: R.P.Z. Project administration: S.E.J.P., M.S.D., W.H.M., S.V.d.R., C.H.B., and R.G.J. Supervision: S.E.J.P., P.B., W.H.M., S.V.d.R., R.P.Z., C.G., C.H.B., and R.G.J. Resources: S.E.J.P., M.S.D., P.B., W.H.M., R.P.Z., R.E.F.G., S.P., and R.G.J. Funding acquisition: P.B., W.H.M., S.V.d.R., C.H.B., and R.G.J. Writing—original draft: S.E.J.P., M.S.D., and S.V.d.R. Writing—review and editing: S.E.J.P., M.S.D., P.B., W.H.M., S.V.d.R., V.R.R., R.E.F.G., and R.G.J. **Competing interests:** C.H.B. is the Chief Scientific Officer of MRM Proteomics and the Chief Lab Analytics Officer of Molecular You. RPX is the Chief Executive Officer of MRM Proteomics Inc. All other authors declare that they have no competing interests. **Data and materials availability:** All data needed to evaluate the conclusions in the paper are present in the paper and/or the Supplementary Materials. The MS proteomics data have been deposited to the ProteomeXchange Consortium via the PRIDE partner repository with the dataset identifier PXD04172. The RNA-seq data have been deposited on the NCBI GEO repository (GSE232359).

Submitted 18 May 2023
Accepted 7 August 2024
Published 13 September 2024
10.1126/sciadv.adi7673